


Review

Controlling the Oxygen Electrocatalysis on Perovskite and Layered Oxide Thin Films for Solid Oxide Fuel Cell Cathodes

Gene Yang ¹, Wonsang Jung ¹, Sung-Jin Ahn ² and Dongkyu Lee ^{1,*} 

¹ Department of Mechanical Engineering, University of South Carolina, Columbia, SC 29208, USA; geney@email.sc.edu (G.Y.); wjung@email.sc.edu (W.J.)

² Energy Lab, Samsung Advanced Institute of Technology, Suwon, Gyeonggi-do 16678, Korea; sjahn.ahn@samsung.com

* Correspondence: dongkyu@cec.sc.edu; Tel.: +1-803-777-0084

Received: 13 February 2019; Accepted: 6 March 2019; Published: 12 March 2019



Abstract: Achieving the fast oxygen reduction reaction (ORR) kinetics at the cathode of solid oxide fuel cells (SOFCs) is indispensable to enhance the efficiency of SOFCs at intermediate temperatures. Mixed ionic and electronic conducting (MIEC) oxides such as ABO_3 perovskites and Ruddlesden-Popper (RP) oxides (A_2BO_4) have been widely used as promising cathode materials owing to their attractive physicochemical properties. In particular, oxides in forms of thin films and heterostructures have enabled significant enhancement in the ORR activity. Therefore, we aim to give a comprehensive overview on the recent development of thin film cathodes of SOFCs. We discuss important advances in ABO_3 and RP oxide thin film cathodes for SOFCs. Our attention is also paid to the influence of oxide heterostructure interfaces on the ORR activity of SOFC cathodes.

Keywords: solid oxide fuel cells; cathodes; oxygen reductions reaction; oxygen surface exchange kinetics; oxide thin films; ABO_3 oxides; Ruddlesden-Popper oxides; heterostructure oxide thin films; strain engineering; oxide interfaces

1. Introduction

Solid oxide fuel cells (SOFCs) have shown great promise to contribute to the ultimate aim of environmentally friendly, efficient energy production and conversion [1–4]. However, overcoming the slow kinetics of the oxygen reduction reaction (ORR) at the cathode is essential to fulfill the increasing demand for developing intermediate temperature SOFCs [5]. At high temperatures such as 1000 °C, $La_{1-x}Sr_xMnO_3$ (LSM_{113}) is commonly used as a cathode for SOFCs owing to their good stability and high electronic conductivity, but simultaneously has low ionic conductivity and a narrow triple-phase boundary (TPB) region for the cathode reaction [1]. Therefore, new cathode materials with faster ORR kinetics are required to facilitate the development of intermediate temperature SOFCs.

Cubic perovskite based mixed ionic and electronic conductors (MIECs) such as ABO_3 oxides [6–9] and layered perovskite based MIECs such as Ruddlesden-Popper (RP) oxides [10–14] have been extensively studied to promote oxygen electrocatalysis at intermediate temperatures such as 600 °C. Compared to LSM_{113} , these MIECs possess considerably higher oxygen surface exchange kinetics, which enables to extend the electrochemically active region to the entire oxide surface from the electrode/electrolyte interface. In addition, they also have higher ionic conductivity than LSM_{113} , and thus are promising cathode materials for intermediate temperature SOFCs. The oxygen diffusion and surface exchange coefficients for ABO_3 and RP oxides are summarized in Table 1.

In ABO_3 and RP oxides, the oxygen ion diffusion and oxygen surface exchange kinetics can be significantly influenced by cation substitution as substitutions on the A or B sites of MIECs are

known to affect the oxygen stoichiometry. For example, substituting Sr for lanthanum on the A-site of $\text{La}_{1-x}\text{Sr}_x\text{CoO}_{3-\delta}$ (LSC₁₁₃) results in an increase in oxygen vacancies, enhancing the oxygen transport and surface exchange kinetics [9,15–19]. In addition, doping with different-size cations in ABO_3 perovskites can also facilitate oxygen migration owing to a reduction in the ion migration energy [20]. The effect of Sr substitution on the activation energy for oxygen ion diffusion and oxygen surface exchange kinetics in LSC₁₁₃, reviewed by Berenov et al. [21], is that the activation energies for oxygen diffusion and surface exchange kinetics decrease with increasing Sr content owing to the reduced vacancy formation energy. Cater et al. [22] compared the oxygen diffusivity between Sr-doped cobaltites and Sr-doped manganites, concluding that B-site cations with a lower valence state increase in oxygen diffusivity. In the case of RP oxides, however, the effect of cation substitutions on the ORR kinetics is poorly understood due to difficulties in synthesizing RP oxides with a wide range of cation substitutions.

Table 1. Oxygen self-diffusion (D^*) and surface exchange coefficients (k^*) for solid oxide fuel cells (SOFC) cathode materials.

Material	$D^*/\text{cm}^2\cdot\text{s}^{-1}$ @ 600 °C	$k^*/\text{cm}\cdot\text{s}^{-1}$ @ 600 °C	Reference
$\text{La}_{0.8}\text{Sr}_{0.2}\text{MnO}_{3-\delta}$	10^{-17}	1.12×10^{-10}	[8]
$\text{La}_{0.5}\text{Sr}_{0.5}\text{MnO}_{3-\delta}$	4.22×10^{-18}	10^{-10}	[8]
$\text{La}_{0.8}\text{Sr}_{0.2}\text{CoO}_{3-\delta}$	1.69×10^{-13}	1.38×10^{-8}	[8]
$\text{La}_{0.6}\text{Sr}_{0.4}\text{CoO}_{3-\delta}$	2.86×10^{-9}	9.09×10^{-8}	[21]
$\text{La}_{0.5}\text{Sr}_{0.5}\text{CoO}_{3-\delta}$	2.51×10^{-10}	3.29×10^{-7}	[8]
$\text{La}_{0.6}\text{Sr}_{0.4}\text{Co}_{0.2}\text{Fe}_{0.8}\text{O}_{3-\delta}$	5.83×10^{-10}	2.35×10^{-7}	[23]
$\text{Ba}_{0.5}\text{Sr}_{0.5}\text{Co}_{0.8}\text{Fe}_{0.2}\text{O}_{3-\delta}$	1.28×10^{-7}	5.21×10^{-5}	[24]
$\text{La}_2\text{NiO}_{4+\delta}$	1.35×10^{-8}	1.02×10^{-6}	[13]
$\text{La}_{1.9}\text{Sr}_{0.1}\text{NiO}_{4+\delta}$	4.66×10^{-9}	3.56×10^{-8}	[13]
$\text{La}_{1.8}\text{Sr}_{0.2}\text{NiO}_{4+\delta}$	2.02×10^{-10}	3.51×10^{-9}	[13]
$\text{La}_2\text{CuO}_{4+\delta}$	2.76×10^{-9}	5.79×10^{-7}	[11]
$\text{La}_2\text{Ni}_{0.9}\text{Co}_{0.1}\text{O}_{4+\delta}$	1.07×10^{-8}	6.52×10^{-7}	[14]
$\text{La}_2\text{Ni}_{0.9}\text{Co}_{0.1}\text{O}_{4+\delta}$	1.34×10^{-8}	7.89×10^{-7}	[14]
$\text{La}_2\text{CoO}_{4+\delta}$	2.98×10^{-8}	3.91×10^{-6}	[25]

All materials are polycrystalline.

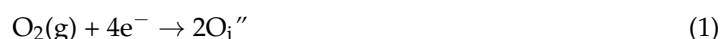
Recently, a remarkable enhancement of the ORR kinetics has been achieved by using epitaxial oxide thin films, which have yielded many intriguing physical and chemical properties that cannot be achieved in bulk counterparts. Epitaxial thin films can also allow the understanding of the fundamental physicochemical properties of oxide materials, and thus have been used as model systems to develop design principles for enhancing the ORR kinetics [26–28]. In particular, the use of oxide thin films has the following advantages for manipulating and evaluating electrocatalytic properties [29]. First, epitaxial thin films can be grown with different orientations, which can allow evaluating anisotropic behaviors (appropriate selection of the single crystal substrates and optimization of the deposition conditions). Second, the termination plane of each surface structure can be controlled using epitaxial thin films, and thus the different surface exchange kinetics can be elucidated. Third, dense thin films can allow studying oxygen transport kinetics with no influence of non-kinetic issues, such as particle morphology and connectivity, and porosity and tortuosity typical in porous electrodes. Lastly, the influence of the strain induced by the substrate on the electrocatalytic properties can be investigated. Furthermore, the use of oxide multilayer heterostructures has opened attractive opportunities in the design of new cathode material systems as oxide interfaces can drastically facilitate the ORR kinetics. So far, oxide heterostructure interfaces have been utilized to achieve unique physical and chemical properties such as phase transition [30], electronic reconstruction [31], magnetic domain rearrangement [32], and anomalous oxygen electrocatalysis [33], which are unattainable in the bulk oxides.

This review aims to provide a synopsis of the major developments and achievements in thin film MIEC cathodes of SOFCs, which can help facilitate the development of intermediate temperature SOFCs. We first discuss the ORR mechanisms on the cathode of SOFCs. We then cover in detail recent advances in ABO₃ and RP oxide thin film cathodes focusing on cobaltites, ferrites, nickelates, and cuprates. The effect of oxide heterostructure interfaces on the ORR kinetics and electrochemical stability is also overviewed. Finally, we present conclusions, perspectives and future developments. As this review deals with mostly epitaxial thin films, we do not focus on the kinetics of oxygen transport. Readers can be referred to relevant comprehensive reviews of oxygen transport in ABO₃ and RP oxide [12,34,35].

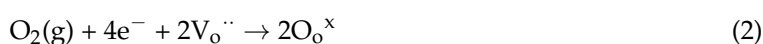
2. Oxygen Reduction in SOFCs

2.1. Oxygen Reduction Reaction Steps and Pathways in SOFC Cathodes

Among the entity of charge transport and transfer processes in an operating SOFC, the activation loss η associated with the ORR at the cathode is a main contribution to the overall voltage drop [36]. In MIEC cathodes, ABO₃ oxides are generally known as oxygen-deficient perovskites because oxygen vacancies are their dominant anion defect while RP oxides can be both oxygen-deficient and oxygen-excess, depending upon their majority oxygen defects. In the case of oxygen-deficient RP oxides, oxygen nonstoichiometry (δ) arises from oxygen vacancies, whereas oxygen interstitials result in oxygen hyperstoichiometric RP oxides. Therefore, two ORR reactions may occur in MIEC cathodes depending on majority oxygen defects [13,37,38]. The overall ORR kinetics for oxygen-excess RP oxides can be expressed as:



where e^- is an electron and $\text{O}_i^{\prime\prime}$ is an oxygen interstitial. Unlike oxygen-excess RP oxides, the following ORR reaction can occur in ABO₃ and oxygen deficient RP oxides.



where $\text{V}_o^{\prime\prime}$ is an oxygen vacancy and O_o^{\times} represents an oxygen ion in the cathode or electrolyte lattice.

However, ORR reaction is composed of numerous elementary reaction steps. These steps can be surface or bulk related reactions such as adsorption, dissociation, electronation, and diffusion (Figure 1). As shown in Figure 1, pure electronic conductors such as Pt and LSM₁₁₃ have the surface pathway for the possible ORR reaction steps, which are adsorption and dissociation of molecular oxygen on the cathode surface, surface diffusion of adsorbed oxygen atoms to the TPB, formation of oxide ions by electron transfer and incorporation into the electrolyte. Previous studies [39–44] identified using polycrystalline LSM₁₁₃ samples that the ORR occurs only at the one-dimensional TPB, where cathode, electrolyte, and gas phase are in contact in pure electronic conductors.

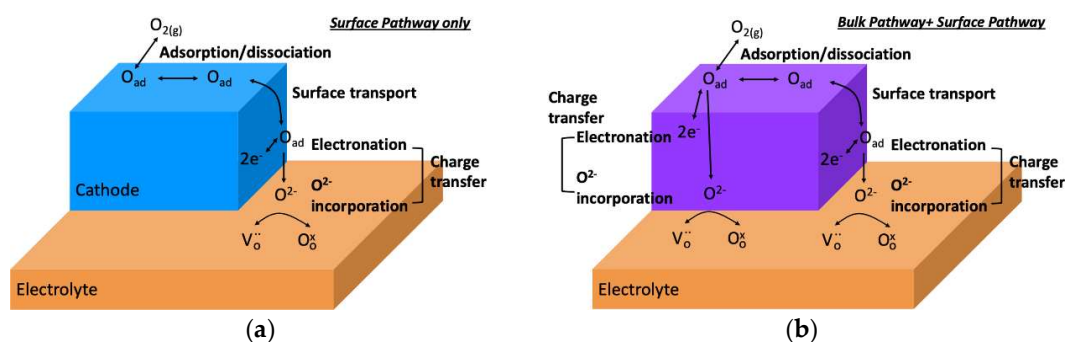


Figure 1. Schematic of possible elementary reaction steps during oxygen reduction reaction (ORR) and possible pathways for two different classes of cathode materials; (a) pure electronic conductor and (b) mixed ionic and electronic conducting (MIEC) cathodes.

In contrast, the surface pathway is complemented by a bulk pathway in MIEC cathodes, where adsorbed oxygen species are reduced at the cathode surface and transported to the electrolyte by solid-state diffusion through the cathode interior regardless of the dominant oxygen defects. Consequently, the active area for the ORR on MIEC cathodes spans over the entire cathode surface. The overall rate of the multitude of reaction steps in MIEC cathodes is determined by a single rate determining step. Then, all remaining steps can be considered to be close to equilibrium so that the voltage loss associated with the rate-determining step constitutes the cathodic activation loss η .

2.2. Oxygen Diffusion and Surface Exchange Kinetics in MIEC Cathodes

The total electrical conductivity σ_{tot} of perovskite oxides can be expressed as:

$$\sigma_{tot} = \sigma_{el} + \sigma_{ion} \quad (3)$$

where σ_{el} and σ_{ion} are electronic conductivity and ionic conductivity, respectively. Depending on the relative amount of σ_{el} and σ_{ion} , perovskite oxides are classified into pure electronic conductors or MIECs.

Oxide cathode materials are typically extrinsic semiconductors, where σ_{el} results from the movement of holes or excited electrons through the surrounding lattice. In addition, MIEC cathodes conduct O^{2-} ions via oxygen vacancies or interstitials at a significant rate. The mobility of O^{2-} ions in MIEC cathodes is correlated with the diffusion coefficient (D^*) for O^{2-} . In addition, the oxygen surface exchange coefficient (k^*) is also a key parameter for determining the rate of oxygen transport through a MIEC cathode material. Therefore, D^* and k^* play a determining role in the ORR kinetics on MIEC cathodes.

In the case of thin film MIEC cathodes, the ORR kinetics can be limited by either oxygen diffusion or oxygen surface exchange kinetics depending on the critical film thickness, t_{crit} , which can be defined as D^*/k^* [45]. The ORR kinetics of thick film cathodes are mainly governed by the bulk transport of oxygen whereas in thin film cathodes the ORR kinetics can be governed by the surface exchange of oxygen. In general, t_{crit} is in the range of 100 μm for many perovskite oxides [46]. Therefore, the ORR kinetics of thin film MIEC cathodes can be enhanced by an increase in the oxygen surface exchange kinetics.

Electrochemical impedance spectroscopy (EIS) measurements are commonly used to analyze the kinetics of oxygen surface exchange on thin film cathodes [6,26,28,47]. Typical EIS tests are conducted in the frequency range from ~ 10 MHz to ~ 100 μHz using an AC voltage amplitude with zero DC bias in a wide range of temperatures and oxygen partial pressures. Without dc bias, the Nyquist plot represents three well-separated features analyzed by an equivalent circuit [48], which are denoted as high frequency (HF), medium frequency (MF) and low frequency (LF) feature. The HF feature (10^4 – 10^5 Hz) is associated with the transport of O^{2-} ions through an electrolyte, while the MF features (10^3 – 10^4 Hz) is associated with the ionic transfer resistance at the electrode/electrolyte interface. In addition, the magnitude of the capacitance at the MF feature is relatively small ($\sim 10^{-6}$ F) compared to the LF feature ($\sim 10^{-3}$ F), which is the main resistive process representing the surface exchange reaction [6,49–52]. In the case of thin film cathodes, the magnitude of capacitance is due to the oxygen content change in the films, and therefore the oxygen surface reaction on thin film electrodes generally corresponds with the LF feature. The electrical oxygen surface exchange coefficient (k^l) can be determined using the expression [53,54],

$$k^l = R \cdot T / 4F^2 \cdot R_{ORR} \cdot A_{electrode} \cdot c_o \quad (4)$$

where R is the universal gas constant ($8.314 \text{ J} \cdot \text{mol}^{-1} \cdot \text{K}^{-1}$), T is the absolute temperature, F is the Faraday's constant ($96,500 \text{ C} \cdot \text{mol}^{-1}$), R_{ORR} is the resistance obtained from the LF feature, $A_{electrode}$ is the area of the electrode, and c_o is the lattice oxygen concentration in thin film cathodes.

3. Thin Film Cathodes

As discussed earlier, the use of epitaxial thin films offers many advantages for controlling the ORR kinetics in SOFC cathodes. Strain engineering is one of the most effective ways to tailor the ORR kinetics of perovskite and layered oxide thin films. Many studies have reported that epitaxial strain strongly influences bulk and surface properties of oxide materials including the electronic structure [55], oxygen transport [56–59], oxygen defect formation [60], and oxygen surface exchange kinetics [61,62], ultimately enhancing the high temperature oxygen electrocatalysis in ABO_3 and RP oxides [63,64]. In addition, the viability of controlling the crystallographic orientation of epitaxial thin films has enabled investigation of the anisotropic nature of oxygen transport and kinetic properties in RP oxides [61,65]. Furthermore, oxide interface engineering has brought a new concept to design highly active and stable cathode materials for intermediate SOFCs [66–68]. The growth of high quality epitaxial thin films is made possible using several deposition methods such as pulsed laser deposition (PLD), molecular beam epitaxy (MBE), atomic layer deposition (ALD), and sputtering. However, it is not the aim of this review to describe in detail those techniques; an extended review on the different techniques can be found elsewhere [69–72]. In the following subsections, we focus on how these factors have brought advances in the oxygen surface exchange kinetics in ABO_3 and RP oxide thin films.

3.1. ABO_3 Oxide Thin Films

ABO_3 perovskite oxides are conventional materials for electrochemical applications, in particular, SOFCs owing to their good reactivity, flexibility in terms of oxygen stoichiometry, and viability of A- and B-site cation substitutions. In most cases, the A-site cation is a combination of rare and alkaline earths for SOFC cathodes. However, the B-site cation is generally a transition metal, such as Mn, Fe, and Co. The atomic structure of perovskites consists in a 3D network of BO_6 octahedra connected by apex, which are maintained by a cubic lattice of A atoms of coordination 12, as shown in Figure 2. The symmetries of ABO_3 perovskites can theoretically be directly determined from the ionic radii of A and B cations, which govern strains inside the materials, since the size mismatch is responsible for the distinct stacking.

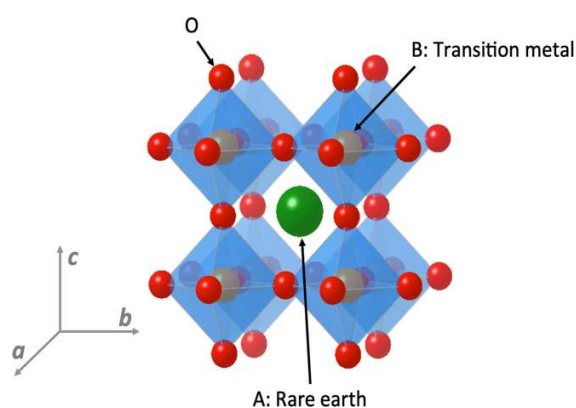


Figure 2. Schematic crystal structure of ABO_3 perovskite oxides, where A and B are a rare earth and transition metal atom.

In the early stage, $LaCoO_3$ (LCO_{113}) [36,73] and $LaMnO_3$ (LMO_{113}) [36,74] based ABO_3 perovskite oxides were utilized as a cathode material for SOFCs. These stoichiometric compositions, however, were found unsuitable in terms of electrochemical performance for a cathode. Usually, the increase of ionic conductivities is more influenced by Sr concentration at the A-site while the increase of the electronic conductivities is more influenced by Fe and Co concentration at the B-site. The substitution of Sr^{2+} for La^{3+} can enhance the oxygen ion transport kinetics due to an increase in the oxygen vacancy concentration in the perovskite structure [17]. Therefore, high electrochemical performance at the cathode could be achieved relative to undoped ABO_3 perovskite oxides. In this sense,

LSC₁₁₃ [17,21,27,28,46,64,73,75,76] and La_{1-x}Sr_xCo_{1-y}F_yO_{3-δ} (LSCF₁₁₃) [22,45,47,66,77–86] perovskite oxides are commonly used as these oxides are known to show oxygen deficiency and the oxygen nonstoichiometry (δ) affects the electrochemical properties, conductivity and lattice expansion of the materials.

3.1.1. Cobaltites

Epitaxial strain induced by lattice mismatch between a thin film and a substrate can effectively control the oxygen migration and oxygen defect formation in ABO₃ perovskite oxides [64,87–93]. Using density functional theory (DFT) calculations, Han et al. [94] demonstrated that tensile strain increased the one-dimensional mobility of oxygen vacancy and adsorbed atomic oxygens migrations on the LCO₁₁₃ surface, which can enhance the ORR kinetics. According to the authors, the maximum tensile strain for the enhanced ORR kinetics is 3%, which has a lower oxygen vacancy formation energy by 0.32 eV compared to the strain-free surface. Later, Mayeshiba and Morgan [90] predicted the oxygen migration barriers in LaMO₃ (M = Sc, Ti, V, Cr, Mn, Fe, Co, Ni, and Ga) perovskite oxides under tensile strain via DFT calculations. They showed that tensile strain can significantly reduce the oxygen migration barriers, resulting in enhanced oxygen diffusion (one order of magnitude) at 500 °C compared with the diffusion under unstrained conditions. laO' et al. [28] experimentally showed that tensile strained epitaxial La_{0.8}Sr_{0.2}CoO_{3-δ} (LSC82) films exhibit significantly increased ORR activity compared to LSC82 bulk. According to the authors, the oxygen surface exchange coefficients (k^f) of epitaxial LSC82 films are about two orders of magnitude higher than those of LSC82 bulk, which is attributed to the increased oxygen vacancy concentration in LSC82 thin film relative to LSC bulk. Using secondary ion mass spectroscopy (SIMS) measurements, Kubicek et al. [64] also investigated the effect of strain on the oxygen surface exchange kinetics of epitaxial LSC82 films. In this work, the epitaxial LSC82 films were synthesized on SrTiO₃ (STO) and LaAlO₃ (LAO) substrates to introduce tensile and compressive strain, respectively, into the LSC82 films, where the oxygen surface exchange kinetics was found to be faster in tensile strained films. The authors postulated that the lower formation energy of oxygen vacancy by tensile strain leads to the enhanced ORR kinetics. However, Crumlin et al. [27] did not observe the strong dependency of the oxygen surface exchange kinetics of epitaxial La_{0.6}Sr_{0.4}CoO_{3-δ} (LSC64) films on strain. The authors attempted to control the degree of tensile strain in LSC64 films with various film thicknesses but the k^f values of LSC64 films were thickness-independent and comparable with those of bulk LSC64 (k^f can be approximated as k^*). Similarly, epitaxial LCO thin films also showed little dependence of their surface exchange kinetics as a function of film thickness although the films exhibited higher ORR kinetics than LCO bulk [95]. In contrast, a clear trend of the thickness-dependent ORR activity in epitaxial LSC64 thin films was recently demonstrated by Lee et al. [96] (Figure 3a). According to this work, the oxygen surface exchange kinetics of LSC64 films can be enhanced as decreasing the film thickness until 50 nm, where strain relaxation occurs. The authors proposed that the increased ORR activity results from the increased oxygen vacancies in epitaxial LSC64 films due to the large tensile strain of high-quality films. Employing in situ impedance spectroscopy during thin film growth, Rupp et al. [97] also showed an enhancement in the oxygen surface exchange kinetics of tensile-strained epitaxial LSC64 films on (001)-oriented La_{0.95}Sr_{0.05}Ga_{0.95}Mg_{0.05}O_{3-δ} substrates compared to unstrained films on yttria-stabilized zirconia (YSZ) substrates. Similar to the results by Lee et al. [96], the authors also found the same trend of enhanced oxygen surface exchange kinetics as film thickness decreases in epitaxial LSC64 films but they interpreted that this trend may be attributed to the capability of in-situ measurement as the films never exposed to any thermal cycling such as cooling from PLD preparation temperature or heating for impedance measurements. However, regardless of strain, epitaxial LSC₁₁₃ thin films were found to have higher k^f values compared to their bulk counterpart (Figure 3b).

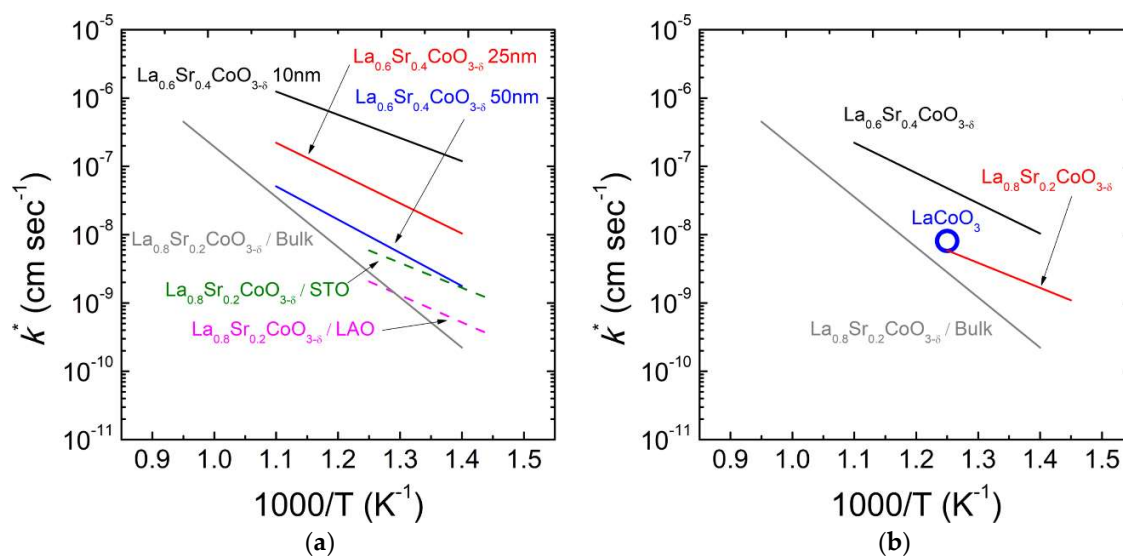


Figure 3. Arrhenius plots of surface exchange coefficients (k^*) for epitaxial $\text{La}_{1-x}\text{Sr}_x\text{CoO}_{3-\delta}$ thin films. (a) Effect of thickness difference on k^* for $\text{La}_{0.6}\text{Sr}_{0.4}\text{CoO}_{3-\delta}$ [96] and of substrate difference (STO and LAO) on k^* for $\text{La}_{0.8}\text{Sr}_{0.2}\text{CoO}_{3-\delta}$ [64] thin films and $\text{La}_{0.8}\text{Sr}_{0.2}\text{CoO}_{3-\delta}$ [9] polycrystalline samples. (b) Effect of Sr substitution on k^* for $\text{La}_{1-x}\text{Sr}_x\text{CoO}_{3-\delta}$ ($x = 0, 0.2$ and 0.4 , [64,95,96]) thin films and $\text{La}_{0.8}\text{Sr}_{0.2}\text{CoO}_{3-\delta}$ [9] polycrystalline oxides.

It is known that lattice strain can tune the electronic structure and charge transfer in ABO₃ oxides [98,99]. Using scanning tunneling spectroscopy and density functional theory calculations, Cai et al. [55] showed that the surface electronic state depends on the strain state of the epitaxial LSC82 thin films. In this work, STO and LAO substrates were utilized to induce tensile and compressive strains, respectively, into the LSC82 films, where tensile-strained LSC films exhibited a more increased electronic density of states (DOS) near the Fermi level compared to compressive strained LSC films. It was hypothesized that the increased DOS and the transition to the metal-like state are attributed to the easier formation of oxygen vacancies on tensile strained LSC films, which was supported by DFT calculations.

A recent study for a wide range of bulk perovskites demonstrated that the position of the oxygen 2p-band center with respect to the Fermi level is linearly correlated with the activation barrier of oxygen surface exchange, acting as a descriptor for the oxygen surface exchange kinetics [100]. According to this work, the formation energy of bulk oxygen vacancies decreases with increasing the oxygen 2p band center relative to the Fermi level, indicating the enhanced oxygen reduction reaction (Figure 4a). Later, Lee et al. [96] demonstrated that the oxygen 2p-band center relative to the Fermi level can be linearly correlated with strain state, where tensile strain results in the upshift of the oxygen 2p-band center (Figure 4b). According to the authors, As the oxygen 2p-band center also has a linear relationship with the vacancy formation energy in perovskite oxides [100], and thus the tensile strain is expected to lower the energy of vacancy formation due to an increase in the oxygen 2p-band center in the LSC₁₁₃ films. Hong et al. [95] showed that in epitaxial LCO₁₁₃ films, strain can be used to reduce the spin transition temperature and promote the occupation of higher spin states that weaken the Co-O bond, which results in an increase in the oxygen surface exchange kinetics. The authors also pointed out that the decreased Co-O bond strength due to the increased fractional occupancy of high-spin states can lead to the oxygen 2p-band center upshift relative to the Fermi energy. Recently, Zhu et al. [101] measured the ORR activities of polycrystalline LSC₁₁₃ thin films with a wide range of Sr concentration ($0 \leq \text{Sr} \leq 0.8$). The authors found that with increasing the Sr content, the O 2p-band center can be close to the Fermi level, which favors the oxygen vacancy formation. However, they claimed that at $\text{Sr} > 0.4$, Co^{2+} becomes optimal for the surface instead of $\text{Co}^{3+}/\text{Co}^{4+}$ and may act as electron traps, which may decrease the electronic conductivity, leading to an overall poor ORR activity of LSC₁₁₃

films. These results showed a different trend with the previously reported data [95,96] which showed enhanced ORR kinetics due to an upshift of the oxygen 2p-band center to the Fermi level.

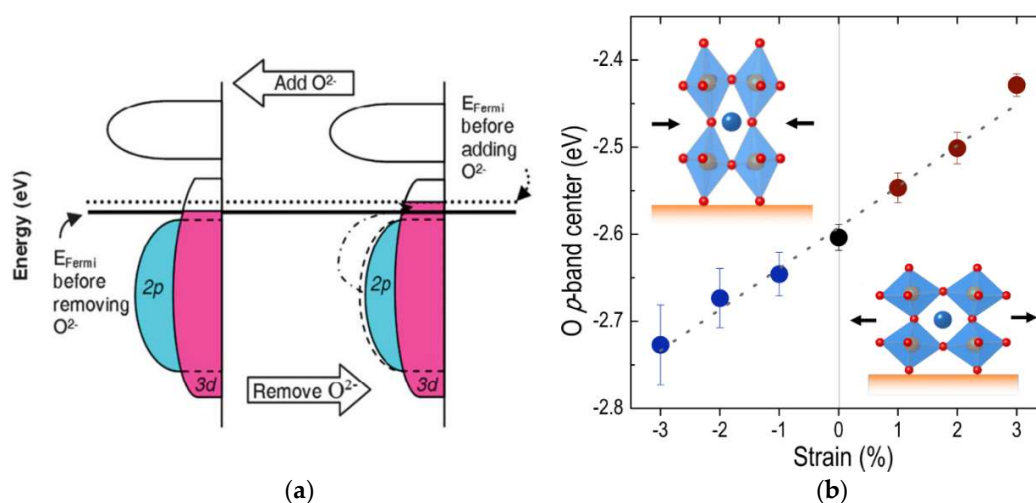


Figure 4. (a) Schematic electronic structure plots to illustrate the correlation of the ORR energetics vs. the O p-band center based on the rigid band model. Reprinted from [100] with permission of The Royal Society of Chemistry. (b) DFT calculations for the oxygen 2p-band center with respect to the Fermi level as a function of strain in LSCO films. The calculated oxygen 2p-band centers are averaged over LSCO films with five different Sr orderings. Reprinted from [96] with permission of The American Chemical Society.

3.1.2. Ferrites

Iron-based perovskites (LaFeO_3 , LFO_{113}) are typically oxygen deficient materials [102,103]. Therefore, LFO_{113} has high oxygen mobility within the material [104] and is suitable for catalytic applications such as oxygen reduction and ion transport in SOFCs [105,106]. Substituting Sr for La on the A-site of LFO_{113} is widely used to promote oxygen defects, enhancing oxygen diffusion and surface exchange processes due to the charge neutrality [107]. However, the ORR activity of $\text{La}_{1-x}\text{Sr}_x\text{FeO}_3$ (LSF_{113}) thin films is still insufficient for the use of oxygen electrocatalysis. For example, using electrochemical impedance spectroscopy (EIS) measurements, la O et al. [108] found that the oxygen surface exchange coefficients (k^{eff}) of $\text{La}_{0.8}\text{Sr}_{0.2}\text{FeO}_3$ (LSF_{82}) thin films are comparable to those of $\text{La}_{0.8}\text{Sr}_{0.2}\text{MnO}_3$ (LSM_{82}) thin films.

Compared to LSF_{113} , LSCF_{113} exhibits better ionic conductivity, reasonable high-temperature stability, and catalytic activity [109–113]. However, there was no systematic study on the strain dependent ORR kinetics (Figure 5a). Baumann et al. [47] and Ingram et al. [85] reported the ORR kinetics of $\text{La}_{0.6}\text{Sr}_{0.4}\text{Co}_{0.8}\text{Fe}_{0.2}\text{O}_{3-\delta}$ (LSCF_{6482}) thin films (Figure 5b). The authors concluded that LSCF_{6428} films can enhance the ORR kinetics compared to bulk LSCF_{6428} due to the increased oxygen vacancies. So far, substantial efforts have been focused on tailoring the surface microstructure of LSCF_{113} thin films to enhance the ORR kinetics, based on the hypothesis that many grain boundaries on the surface of LSCF_{113} films may modify the oxygen bulk diffusion and catalytic properties to enhance the ORR kinetics. For instance, Prestat et al. [114] investigated the ORR kinetics of $\text{La}_{0.52}\text{Sr}_{0.48}\text{Co}_{0.18}\text{Fe}_{0.82}\text{O}_{3-\delta}$ thin films with various thicknesses (Figure 5b). In this study, the polarization resistance of LSCF films was reduced by decreasing the film thickness, indicating that the number of grain boundaries on the surface increases. Consequently, the oxygen surface exchange and diffusion coefficients were significantly enhanced in LSCF thin films compared to bulk LSCF [84]. Angoua et al. [115] investigated the ORR kinetics of LSCF_{6428} thin films with a $\text{Ce}_{0.8}\text{Gd}_{0.2}\text{O}_{1.9}$ (CGO) layer. Adding CGO to LSCF_{6428} films reduced the polarization resistance for LSCF-CGO films, which leads to a higher density of grain boundaries. Bagarinao et al. [116] discussed the oxygen surface exchange and diffusion kinetics of LSCF_{6428} thin films by comparing a nanograined microstructure

film. The authors found that introducing grain boundaries on LSCF6428 films can enhance the oxygen surface exchange reactivity, which is in good agreement with previously reported data [115].

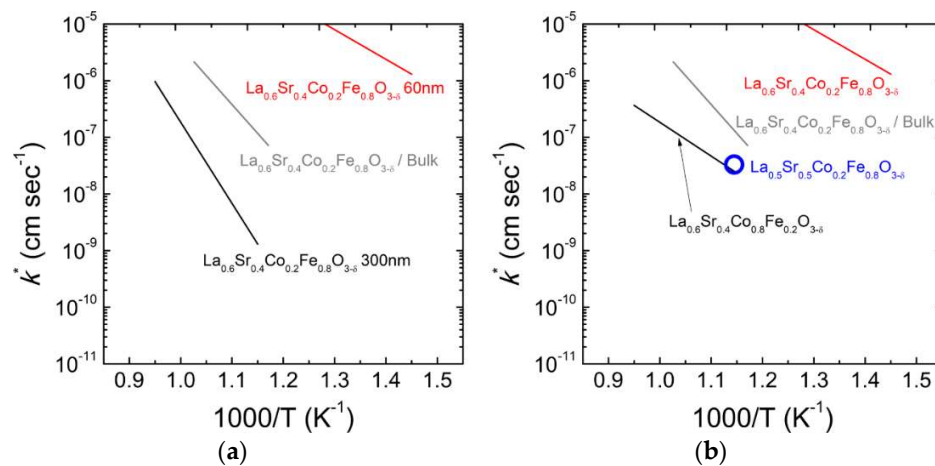


Figure 5. Arrhenius plots of surface exchange coefficients (k^*) for $\text{La}_{1-x}\text{Sr}_x\text{Co}_{1-y}\text{Fe}_y\text{O}_{3-\delta}$ thin films. (a) Effect of strain on k^* for $\text{La}_{0.6}\text{Sr}_{0.4}\text{Co}_{0.2}\text{Fe}_{0.8}\text{O}_{3-\delta}$ [117] and $\text{La}_{0.6}\text{Sr}_{0.4}\text{Co}_{0.2}\text{Fe}_{0.8}\text{O}_{3-\delta}$ [118] films and $\text{La}_{0.6}\text{Sr}_{0.4}\text{Co}_{0.2}\text{Fe}_{0.8}\text{O}_{3-\delta}$ (Ref. [119]) polycrystalline samples. (b) Effect of Sr substitution on k^* for $\text{La}_{1-x}\text{Sr}_x\text{Co}_{1-y}\text{Fe}_y\text{O}_{3-\delta}$ (red [117], black [47] and blue [114]) films and $\text{La}_{0.6}\text{Sr}_{0.4}\text{Co}_{0.2}\text{Fe}_{0.8}\text{O}_{3-\delta}$ [119] polycrystalline oxides.

It was also shown that the ORR kinetics can be enhanced by using the LSCF₁₁₃ thin film as an interfacial layer at the electrode-electrolyte interface. Dumaisnil et al. [120] investigated the ORR kinetics of adding LSCF6482 thin films between porous LSCF113 cathode and Gd-doped ceria (GDC) substrate. In this study, the addition of LSCF6482 thin films was found to result in lower polarization resistance, which may be attributed to the increased active area due to the enhanced adhesion between cathode/substrate. Jang et al. [121] also investigated the ORR kinetics by addition of porous nanoparticle network structured LSCF6428 thin film between the cathode and electrolyte. The cell with LSCF6428 films showed higher peak power density and smaller polarization resistance compared to the cell without LSCF6428 film. Later, the role of nanoparticle network structured LSCF6428 thin film, which is called nano-web structured LSCF6428 (NW-LSCF) was further discussed [122].

3.2. Ruddlesden-Popper (RP) Oxides

The general formula of Ruddlesden-Popper (RP) phases can be written as $\text{A}_{n+1}\text{B}_n\text{O}_{3n+1}$ [123]. The RP phases are comprised of n consecutive perovskite layers (ABO_3) alternating with rock-salt layers (AO) along the crystallographic c -axis direction. Their formula can be represented by $(\text{AO})(\text{ABO}_3)_n$, where n represents the number of connected layers of vertex sharing BO_6 octahedra [124]. In the case of SOFCs, the $n = 1$ members of some RP series, notably those based on $\text{La}_2\text{NiO}_{4+\delta}$ (LNO_{214}) are of particular interest. These RP oxides were shown to accommodate oxygen interstitials in the AO layers [10], leading to fast ion conduction and hence potential application as cathodes at intermediate temperatures. Recently, lanthanum strontium cobaltites have attracted much attention as a cathode material for SOFCs, which exhibited interestingly fast oxygen exchange kinetics when interfaced with its perovskite counterpart LSC₁₁₃ [67,125]. In addition, $(\text{La,Sr})_2\text{CuO}_4$ (LSCu_{214}) has also demonstrated its availability as a promising cathode for SOFCs showing comparable oxygen surface exchange kinetics to that of LSCF₁₁₃ thin films at intermediate temperatures [126]. Figure 6 presents the ideal tetragonal unit-cells for $n = 1$, which correspond to the stoichiometric compounds all of same space group, $I4/mmm$.

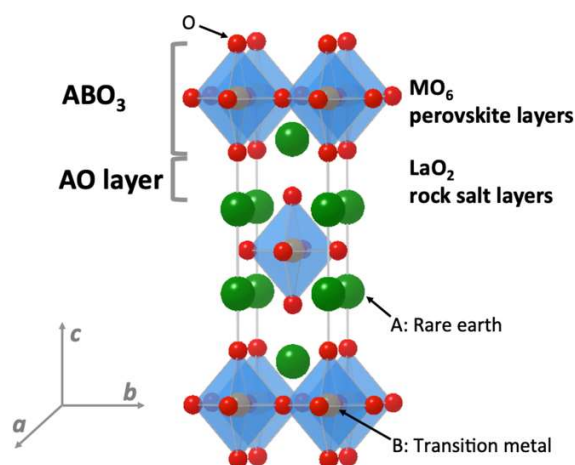


Figure 6. Schematic crystal structure of RP oxides, where A and B are a rare earth and transition metal atom.

It is well-known that RP oxides exhibit strong anisotropic features as a result of the adjustment of two different structural units, i.e., ABO₃ and AO within the lattice. While the B-site cations are coordinated by six oxygen anions, the B-O bond lengths are different due to the Jahn-Teller effect caused by the valence state of the B-site cations [127]. This results in two types of oxygen species in the BO₆ octahedra, which are referred to as “apical” and “equatorial” oxygen. In the RP system, interstitial sites are located in the AO layer, where RP oxides can accommodate an excess oxygen as an interstitial oxygen defect. Oxygen vacancies can also be formed by appropriate doping in the system. Consequently, the oxygen transport properties of RP oxides can be strongly influenced by either oxygen interstitials or oxygen vacancies as discussed earlier.

Nickelates are interesting alternative materials to LSC₁₁₃ for intermediate temperature SOFCs owing to its high oxygen surface exchange kinetics and oxygen transport properties [10,11,13,14,61,128–133]. However, due to difficulties in synthesizing epitaxial thin films of nickelates, few studies have examined the ORR kinetics of nickelates in a form of epitaxial films. Yamada et al. [134] first reported the oxygen electrocatalysis of epitaxial RP oxide thin films using (011)-oriented epitaxial Nd₂NiO_{4+δ} (NNO₂₁₄) films on (001) YSZ substrates. According to this study, compression along the c-axis of NNO₂₁₄ films reduces the oxygen surface exchange kinetics. Later, Tsvetkov et al. [135] compared the δ values of tensile- and compressive-strained NNO₂₁₄ thin films, demonstrating that the larger δ in tensile-strained NNO₂₁₄ can enhance the oxygen surface exchange kinetics relative to those of compressive-strained NNO₂₁₄ thin films (Figure 7a). These results are in good agreement with the previous observation by Yamada et al. [134].

Among various RP oxides, LNO₂₁₄ is the most widely studied member of the series. Kim et al. [136] proposed that epitaxial LNO₂₁₄ thin films with a thickness of 300 nm may possess two different surface exchange rates as a result from the coexistence of two different film microstructures. Later, they demonstrated that the surface exchange reaction of polycrystalline LNO₂₁₄ samples limits the electrode reaction, showing comparable *k^{eff}* values with those obtained previously for LNO₂₁₄ bulk [132]. However, to evaluate the effect of strain on the ORR kinetics in RP oxides, high quality epitaxial thin films are required. Burriel and co-workers [61] synthesized (001)-oriented epitaxial LNO₂₁₄ thin films on STO and NbGaO₃ (NGO) substrates, which introduce tensile and compressive strain states, respectively, into the LNO₂₁₄ films. They evaluated the oxygen diffusion and surface exchange kinetics for tensile- and compressive-strained LNO₂₁₄ films, concluding that both compressive and tensile strain led to a reduction in the oxygen diffusivity in the first 175–200 nm of the film, whereas neither strain affected the oxygen surface exchange. However, Lee et al. [63] later demonstrated that tensile strain along the c-direction can lead to an increase in the driving force to form interstitial oxygen atoms in LNO₂₁₄, resulting in enhanced oxygen surface exchange kinetics of (100)-oriented epitaxial LNO₂₁₄ thin films (Figure 7b). In this study, the authors successfully controlled

strain in LNO₂₁₄ films by modulating the film thickness. The discrepancy in the effects of strain on oxygen surface exchange kinetics in LNO₂₁₄ films may be attributed to the fact that the critical thickness required to maintain an acceptable strain state is fairly smaller than what Burriel et al. [61] used. However, the effect of strain on the ORR kinetics in RP oxides needs further investigation.

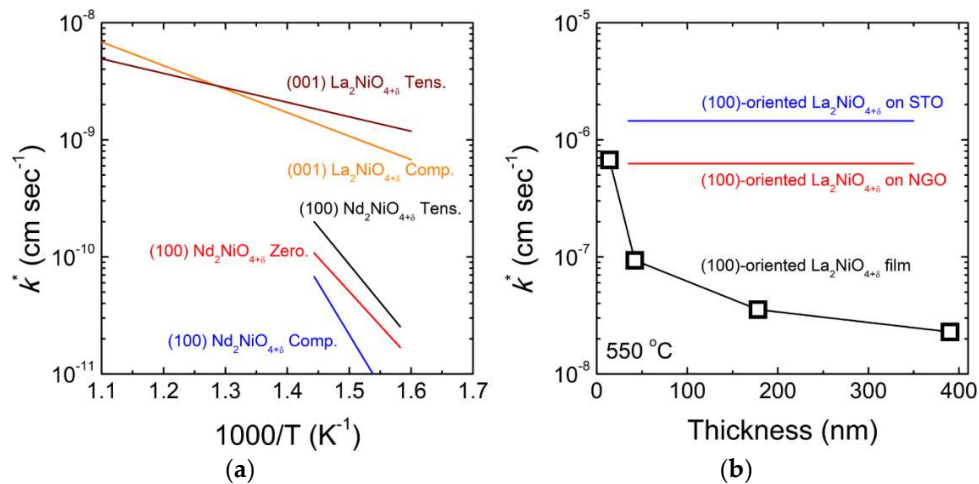


Figure 7. Arrhenius plots of surface exchange coefficients (k^*) for $A_2NiO_{4+\delta}$ ($A = La$ and Nd): (a) Tensile (Tens.) and compressive (Comp.) strained (001)-oriented $La_2NiO_{4+\delta}$ films [61] and tensile, zero, and compressive strained (100)-oriented $Nd_2NiO_{4+\delta}$ thin films [135]; (b) (001)- and (100)-oriented $La_2NiO_{4+\delta}$ [61,63] thin films with various thickness and substrates.

Similar to the correlation between the oxygen 2p-band center and ORR kinetics in ABO_3 oxides, Lee et al. [126] also proposed that the oxygen 2p-band center relative to the Fermi energy can be an effective descriptor to predict the oxygen surface exchange as well as the activation energy for oxygen transport in RP oxides. In contrast to ABO_3 oxides, the oxygen 2p-band center relative to the Fermi level was found to be inversely proportional to the oxygen surface exchange kinetics in RP oxides (Figure 8). According to the authors, the opposite slopes of the oxygen 2p-band center correlations between the RP oxides and the perovskite materials are due to the intrinsic mechanistic differences of their oxygen surface exchange kinetics and bulk anionic transport. The authors also found that the calculated interstitial formation energies of $La_2BO_{4+\delta}$ ($B = Co, Ni, \text{ and } Cu$) strongly depend on the B cation in the sequence $LCuO_{214} > LNO_{214} > LCO_{214}$, which corresponds to the trend of B-cation-dependent oxygen diffusivity. Recently, Xie et al. [137] also calculated the formation energy of oxygen interstitials in the same RP oxide systems, demonstrating that, regardless of δ , the formation energy of oxygen interstitials decreases with decreasing the atomic number of the B cation, which is in good agreement with the data reported by Lee et al. [126].

As discussed earlier, the anisotropy of oxygen migration is one of the intrinsic properties of RP oxides owing to its structural feature. Therefore, different oxygen diffusion and surface exchange kinetics along different crystallographic directions were reported as shown in Figure 9. Using NNO_{214} and $Pr_2NiO_{4+\delta}$ (PNO_{214}) single crystalline oxides, Bassat et al. [128] observed a large anisotropy for the oxygen surface exchange kinetics for both oxides, where the k^* values in the a - b plane are 1.5 orders of magnitude larger than those along the c -axis. Burriel et al. [61] reported that the oxygen diffusion and oxygen surface exchange kinetics in the a - b plane are faster than those along the c -direction in epitaxial LNO₂₁₄ thin films. However, later the authors also evaluated the anisotropy for the oxygen surface exchange kinetics of LNO₂₁₄ single crystalline, reporting the lack of anisotropy in the oxygen surface exchange values, which is attributed to the surface segregation process [133]. The anisotropy of the oxygen surface exchange kinetics was also observed in Sr-doped LNO₂₁₄ films. Lee et al. [65] demonstrated that substituting Sr for lanthanum in LSNO₂₁₄ thin films can result in the structural

reorientation of the films because of the reduction in the surface energy of the (001) surface, reporting the anisotropic oxygen surface exchange kinetics.

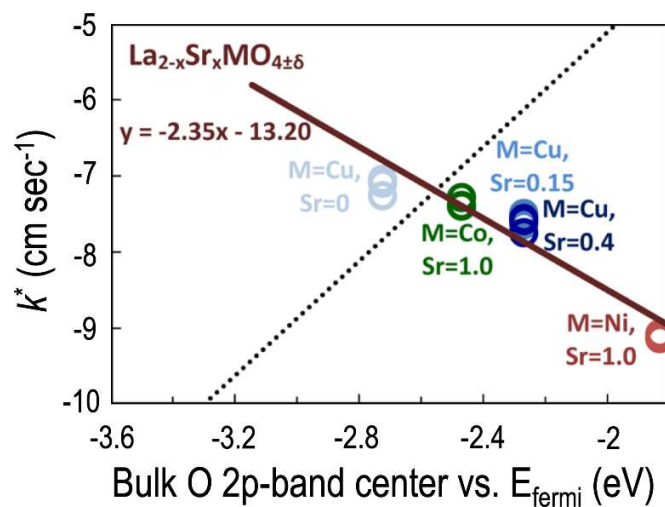


Figure 8. Oxygen surface exchange coefficients (k^*) of La_2CuO_4 (light blue), LaSrCoO_4 (green), $\text{La}_{1.85}\text{Sr}_{0.15}\text{CuO}_4$ (blue), $\text{La}_{1.6}\text{Sr}_{0.4}\text{CuO}_4$ (dark blue), and LaSrNiO_4 (red) films with (001) orientations measured at 550 °C versus the computed DFT bulk O 2p-band centers (relative to the Fermi level, E_{Fermi}). The gray dashed lines represent the correlation between experimental oxygen surface-exchange coefficients and the computed bulk O 2p-band centers for a series of SOFC perovskites. Reprinted from [126] with permission of The American Chemical Society.

$\text{La}_{2-x}\text{Sr}_x\text{CuO}_{4\pm\delta}$ (LSCu_{214}) oxides are famous for their high T_c superconductivity [138–140]. Interestingly, the superconducting properties of LSCu_{214} depend on the Sr concentration and oxygen stoichiometry, which also strongly influence the kinetics of oxygen exchange and oxygen diffusion. Opila et al. reported the anisotropic oxygen transport properties and proposed the defect model for Sr-doped cuprates [38,141]. Recently, using epitaxial LSCu_{214} thin films, the oxygen surface exchange kinetics were evaluated at intermediate temperatures [126]. In this study, the k^* values of undoped La_2CuO_4 (LCuO_{214}) thin films were found to be higher than those of Sr-doped La_2CuO_4 thin films (Figure 9a), which is attributed to that adding Sr content resulted in changes of the oxygen 2p-band center relative to the Fermi energy. More recently, Meyer and co-workers [142] revealed that the oxygen nonstoichiometry commonly reported for strained LSCu_{214} is mediated by the strain-modified surface exchange kinetics, rather than reduced thermodynamic oxygen formation energies. The authors also demonstrated that tensile-strained LSCu_{214} shows nearly an order of magnitude faster oxygen exchange rate in tensile-strained LSCu_{214} films compared to a compressively strained film.

$\text{La}_{2-x}\text{Sr}_x\text{CoO}_{4\pm\delta}$ (LSC_{214}) oxides are widely used as a perovskite counterpart to promote the oxygen electrocatalysis of ABO_3 perovskite such as LSC_{113} [33,68,125,143]. However, LSC_{214} showed very attractive transport and surface exchange properties at intermediate temperatures. For instance, $\text{La}_2\text{CoO}_{4\pm\delta}$ (LCO_{214}) showed higher oxygen diffusivity and lower activation energy in the temperature range of 450–700 °C as compared to nickelates and cuprates [11,13,25]. Later, Lee et al. [126] calculated the interstitial formation energies of LCO_{214} , LNO_{214} , and LCuO_{214} and found the minimum energy for interstitial formation in LCO_{214} . In addition, the authors also reported that the k^* values of LSC_{214} thin films are comparable to LSC_{113} thin films, indicating a promising alternative cathode material to LSC_{113} . Recently, Chen et al. [144] successfully fabricated LSC_{214} ($\text{Sr} = 0.25$) thin films grown in two different crystallographic orientations, i.e., (100) and (001), using (100) LaSrAlO_4 (LSAO) and (001) SrTiO_3 (STO) substrates. They demonstrated that the oxygen diffusivity along the a - b plane in the (100)-oriented LSC_{214} film was three orders of magnitude lower than that in the (001)-oriented LSC_{214} film (Figure 9b). Moreover, the D^* value along the c -direction in the (001)-oriented LSC_{214} film was found to be one order of magnitude higher than that along the a - b plane in the (100)-oriented

LSC₂₁₄ film. However, no dependence of oxygen surface exchange kinetics was observed on the crystal orientation, which may be attributed to the strong Sr segregation at the surface overriding the effect of the structural anisotropy.

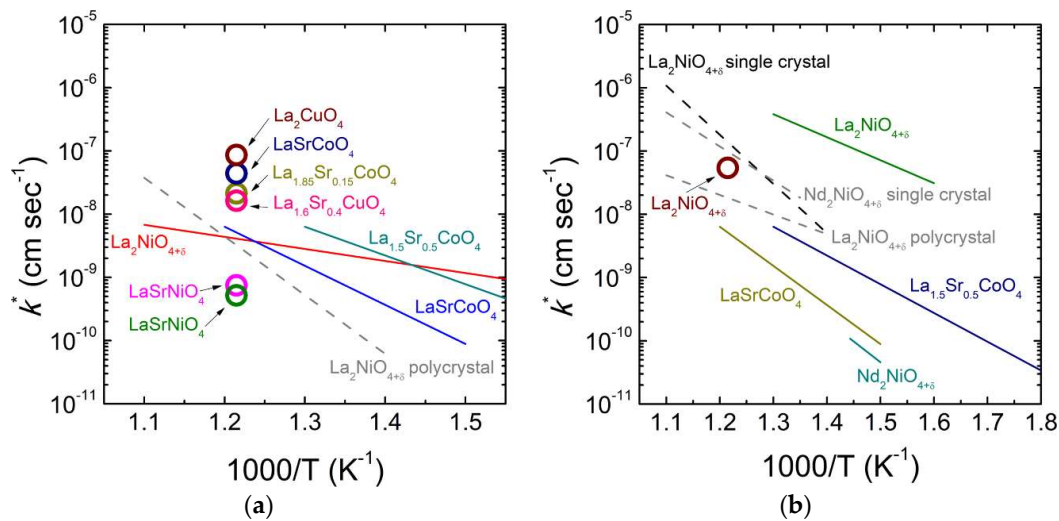


Figure 9. Arrhenius plots of surface exchange coefficients (k^*) for different RP oxides: (a) k^* along c-direction in $\text{La}_{2-x}\text{Sr}_x\text{MO}_4$ (M = Cu, Co, Ni, [126,133,135,144]); and (b) k^* along a-b plane in $\text{A}_{2-x}\text{Sr}_x\text{MO}_4$ (A = Sr, La, Nd and M = Co, Ni, [61,65,128,133,135,144]) thin films.

3.3. Oxide Heterostructure Interface

To achieve enhanced surface exchange kinetics and stability, recent efforts have been focused on developing advanced cathode materials based on MIECs with surface modification [27,33,66,68,76,82,86,125,143,145–148]. Oxide heterostructure interfaces, the combination of a Ruddlesden-Popper (RP, LSC₂₁₄) layer on top of the perovskite LSC₁₁₃, have shown remarkably high oxygen surface exchange kinetics [27,33,68,86,125,143,148,149]. Yashiro et al. reported ~1 order of magnitude enhancement in activity for the composite cathode screen-printed with the mixture of LSC64 and LSC₂₁₄ [143]. Sase et al. [33] have also reported ~3 orders of magnitude higher oxygen surface exchange coefficient (k^*) at the interfacial region between polycrystalline LSC64 and LSC₂₁₄ compared to their bulk value [21]. Later, Crumlin et al. [27,148] utilized epitaxial LSC₁₁₃ and LSC₂₁₄ thin films, achieving higher oxygen surface exchange coefficients of LSC₁₁₃. Recently, Zhao et al. [150] also observed ~10 times higher k^* values in heterostructure LSC₁₁₃/LSC₂₁₄ thin films than those in LSC₁₁₃, which is attributed to increased number of active oxygen vacancies that manipulate the oxygen 2p-band center.

A recent study using Coherent Bragg Rod Analysis (COBRA) revealed the atomic structure and concentrations of the (001)-oriented LSC₁₁₃ thin film on a STO substrate, which shows strontium (Sr) segregation toward the LSC₁₁₃ surface and Sr depletion near the interface between LSC₁₁₃ and STO [151]. It was also reported that heating the (001)-oriented LSC₁₁₃ surface leads to the formation of surface Sr-enriched particles upon annealing while the LSC₂₁₄-decorated LSC₁₁₃ surface chemistry is stable upon heating [152]. More recently, Lee et al. [86] compared the time-dependent surface exchange kinetics and stability of epitaxial LSCF₁₁₃ and LSC₁₁₃ thin films with LSC₂₁₄ surface decoration. Using density functional theory (DFT) computation, the authors revealed greater surface Sr segregation for LSCF₁₁₃, which is predicted to have an SrO termination, than LSC₁₁₃, which is predicted to have a less Sr enriched ($\text{La}_{0.25}\text{Sr}_{0.75}\text{O}$) termination. Furthermore, the authors pointed out a lower energy gain to move Sr from LSCF₁₁₃ into LSC₂₁₄ relative to the LSC₂₁₄-LSC₁₁₃ surface (Figure 10). These observations have suggested that the surface decoration can modulate the surface Sr segregation and the surface phase stability, which can greatly influence the oxygen surface exchange kinetics and the surface stability in LSC₁₁₃ and LSCF₁₁₃. Therefore, understanding the surface decoration effect on the surface

chemistry of perovskites is critical and other potential surface modification materials need to be investigated to design highly active and stable cathodes for SOFCs.

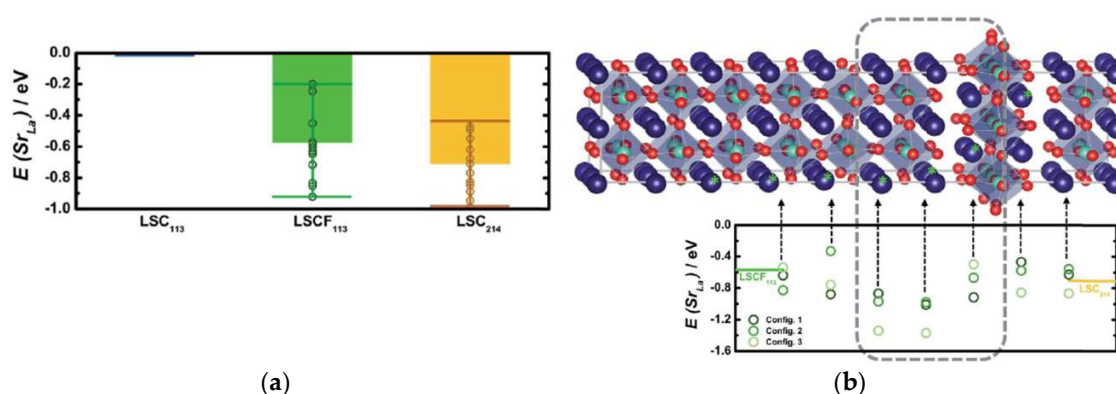


Figure 10. (a) The calculated Sr/La substitution energies in the bulk LSC₂₁₄, LSC₁₁₃, and LSCF₁₁₃ (all relative to that of LSC₁₁₃, which is set to 0). (b) The heterostructured interface model used in the DFT simulations and the results of Sr/La substitution energies. The elements are represented as: La/Sr (dark blue), Fe/Co (light blue, center of the octahedra), and O (red). Reprinted from [86] with permission of The Royal Society of Chemistry.

Similar to the LSC₁₁₃ surface modification with LSC₂₁₄, several studies have also reported the enhanced surface electrocatalytic activity of porous LSCF cathodes with surface decoration [82,147,153,154]. For example, depositing thin La_{0.85}Sr_{0.15}MnO_{3- δ} coatings on porous LSCF6428 electrodes using an infiltration process, Lynch et al. [82] showed the enhanced surface electrocatalytic activity of decorated LSCF₁₁₃ cathodes upon polarization. Vast majority of research has been performed on porous LSCF₁₁₃ electrodes, which lead to ambiguous structure and geometry, and therefore the physical origin responsible for enhanced cathodic performance associated with surface decoration of perovskites is not yet completely understood. However, Lee et al. [66] recently demonstrated using new forms of heterostructure oxide interfaces—(1) LSCF6428 thin films with a single layer decoration of mixed LSC₂₁₄ and LSC₁₁₃ and (2) LSCF6428 thin films with a double layer decoration of stacked LSC₂₁₄ and LSC₁₁₃ – significantly enhanced ORR activity of LSCF6428. More recently, Chen et al. [155] showed the improved electrocatalytic activity and durability of LSCF6428 thin films by coating PrO₂. The authors claimed that PrO₂ coating facilitates the rate of oxygen dissociation due to increased oxygen vacancies. Figure 11 shows the influence of heterointerfaces on k^* for LSC₁₁₃ and LSCF₁₁₃.

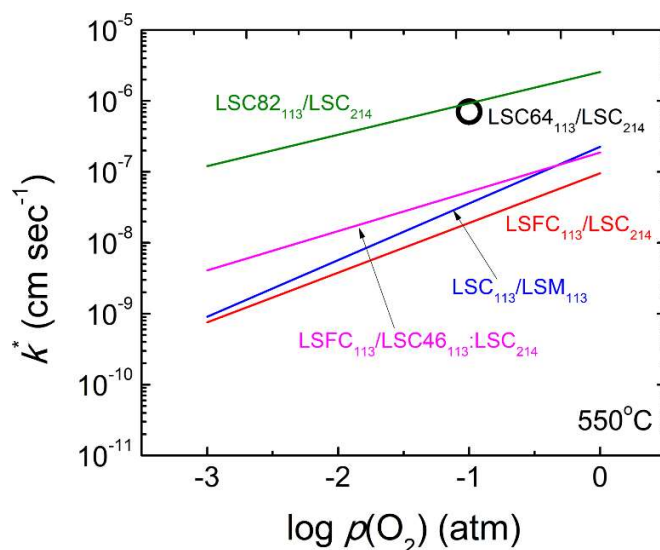


Figure 11. Arrhenius plots of surface exchange coefficients (k^*) for various heterostructure oxide thin films. Effect of heterostructure interfaces on k^* for $\text{La}_{0.6}\text{Sr}_{0.4}\text{CoO}_{3-\delta}/(\text{LaSr})_2\text{CoO}_{4\pm\delta}$ [150], $\text{La}_{0.625}\text{Sr}_{0.375}\text{Fe}_{0.75}\text{Co}_{0.25}\text{O}_{3-\delta}/(\text{LaSr})_2\text{CoO}_{4\pm\delta}$ [86], $\text{La}_{0.8}\text{Sr}_{0.2}\text{CoO}_{3-\delta}/\text{La}_{0.8}\text{Sr}_{0.2}\text{MnO}_{3-\delta}$ [76], $\text{La}_{0.8}\text{Sr}_{0.2}\text{CoO}_{3-\delta}/(\text{LaSr})_2\text{CoO}_{4\pm\delta}$ [148] and $\text{La}_{0.6}\text{Sr}_{0.4}\text{Fe}_{0.8}\text{Co}_{0.2}\text{O}_{3-\delta}/\text{La}_{0.4}\text{Sr}_{0.6}\text{CoO}_{3-\delta}:(\text{LaSr})_2\text{CoO}_{4\pm\delta}$ [66].

4. Conclusions

Developing intermediate temperature SOFCs requires discovering new cathode materials with faster ORR kinetics. MIEC oxides such as ABO_3 oxides and RP oxides are promising alternative cathode materials to LSM113, pure electronic conductor. Recently, introducing oxide thin films and oxide heterostructure interfaces has been recognized as an extremely effective means to control the ORR kinetics of MIEC oxides, opening a plethora of new possibilities useful for intermediate temperature SOFCs. We have briefly overviewed how epitaxial strain can influence the oxygen surface exchange kinetics in ABO_3 and RP oxide thin films. It has been pointed out that strain can tune the oxygen 2p-band center relative to the Fermi energy as a result of the modulated concentration of oxygen defects. In the case of RP oxides, epitaxial thin films offer a direct way to evaluate the intrinsic anisotropy of oxygen diffusion and surface exchange kinetics. Lastly, oxide heterointerfaces can be used to improve the ORR kinetics and stability of ABO_3 oxides. This review has given a comprehensive overview of the current state of research. However, a full understanding of the effect of strain and crystallographic orientation on the ORR kinetics in ABO_3 and RP oxides is still being developed for intermediate SOFCs. In addition, understanding the surface decoration effect on the surface chemistry of perovskites and other potential surface modification materials still need to be investigated to design highly active and stable cathodes for SOFCs.

Author Contributions: D.L. conceived and coordinated the whole idea of writing this paper. G.Y. and W.J. identified the most active and promising research topics in the field under review and analyzed the selected scientific literature. S.-J.A. consulted the relevant studies and references. All the authors contributed to the writing of the manuscript.

Funding: This research was funded by Advanced Support Program for Innovative Research Excellence-I funding (#15540-18-47811) provided by the Office of the Vice President for Research at the University of South Carolina.

Conflicts of Interest: The authors declare no conflict of interest.

References

- Adler, S.B. Factors governing oxygen reduction in solid oxide fuel cell cathodes. *Chem. Rev.* **2004**, *104*, 4791–4843. [[CrossRef](#)] [[PubMed](#)]
- Jacobson, A.J. Materials for solid oxide fuel cells. *Chem. Mater.* **2010**, *22*, 660–674. [[CrossRef](#)]

3. Shao, Z.P.; Haile, S.M. A high-performance cathode for the next generation of solid-oxide fuel cells. *Nature* **2004**, *431*, 170–173. [[CrossRef](#)] [[PubMed](#)]
4. Steele, B.C.H.; Heinzel, A. Materials for fuel-cell technologies. *Nature* **2001**, *414*, 345–352. [[CrossRef](#)]
5. Wachsman, E.D.; Lee, K.T. Lowering the temperature of solid oxide fuel cells. *Science* **2011**, *334*, 935–939. [[CrossRef](#)] [[PubMed](#)]
6. Kawada, T.; Suzuki, J.; Sase, M.; Kaimai, A.; Yashiro, K.; Nigara, Y.; Mizusaki, J.; Kawamura, K.; Yugami, H. Determination of oxygen vacancy concentration in a thin film of $\text{La}_{0.6}\text{Sr}_{0.4}\text{CoO}_{3-\delta}$ by an electrochemical method. *J. Electrochem. Soc.* **2002**, *149*, E252–E259. [[CrossRef](#)]
7. Mizusaki, J.; Mima, Y.; Yamauchi, S.; Fueki, K.; Tagawa, H. Nonstoichiometry of the perovskite-type oxides $\text{La}_{1-x}\text{Sr}_x\text{CoO}_{3-\delta}$. *J. Solid State Chem.* **1989**, *80*, 102–111. [[CrossRef](#)]
8. De Souza, R.A.; Kilner, J.A. Oxygen transport in $\text{La}_{1-x}\text{Sr}_x\text{Mn}_{1-y}\text{Co}_y\text{O}_{3\pm\delta}$ perovskites: Part II. Oxygen surface exchange. *Solid State Ion.* **1999**, *126*, 153–161. [[CrossRef](#)]
9. De Souza, R.A.; Kilner, J.A. Oxygen transport in $\text{La}_{1-x}\text{Sr}_x\text{Mn}_{1-y}\text{Co}_y\text{O}_{3\pm\delta}$ perovskites: Part I. Oxygen tracer diffusion. *Solid State Ion.* **1998**, *106*, 175–187. [[CrossRef](#)]
10. Bassat, J.M.; Odier, P.; Villesuzanne, A.; Marin, C.; Pouchard, M. Anisotropic ionic transport properties in $\text{La}_2\text{NiO}_{4+\delta}$ single crystals. *Solid State Ion.* **2004**, *167*, 341–347. [[CrossRef](#)]
11. Boehm, E.; Bassat, J.M.; Steil, M.C.; Dordor, P.; Mauvy, F.; Grenier, J.C. Oxygen transport properties of $\text{La}_2\text{Ni}_{1-x}\text{Cu}_x\text{O}_{4+\delta}$ mixed conducting oxides. *Solid State Sci.* **2003**, *5*, 973–981. [[CrossRef](#)]
12. Lee, D.; Lee, H. Controlling oxygen mobility in Ruddlesden–Popper oxides. *Materials* **2017**, *10*, 368. [[CrossRef](#)]
13. Boehm, E.; Bassat, J.M.; Dordor, P.; Mauvy, F.; Grenier, J.C.; Stevens, P. Oxygen diffusion and transport properties in non-stoichiometric $\text{Ln}_{2-x}\text{NiO}_{4+\delta}$ oxides. *Solid State Ion.* **2005**, *176*, 2717–2725. [[CrossRef](#)]
14. Kilner, J.A.; Shaw, C.K.M. Mass transport in $\text{La}_2\text{Ni}_{1-x}\text{Co}_x\text{O}_{4+\delta}$ oxides with the K_2NiF_4 structure. *Solid State Ion.* **2002**, *154–155*, 523–527. [[CrossRef](#)]
15. Ishigaki, T.; Yamauchi, S.; Kishio, K.; Mizusaki, J.; Fueki, K. Diffusion of oxide ion vacancies in perovskite-type oxides. *J. Solid State Chem.* **1988**, *73*, 179–187. [[CrossRef](#)]
16. Ishigaki, T.; Yamauchi, S.; Mizusaki, J.; Fueki, K.; Tamura, H. Tracer diffusion-coefficient of oxide ions in LaCoO_3 single-crystal. *J. Solid State Chem.* **1984**, *54*, 100–107. [[CrossRef](#)]
17. Mizusaki, J. Nonstoichiometry, diffusion, and electrical-properties of perovskite-type oxide electrode materials. *Solid State Ion.* **1992**, *52*, 79–91. [[CrossRef](#)]
18. Routbort, J.L.; Doshi, R.; Krumpelt, M. Oxygen tracer diffusion in $\text{La}_{1-x}\text{Sr}_x\text{CoO}_3$. *Solid State Ion.* **1996**, *90*, 21–27. [[CrossRef](#)]
19. VanDoorn, R.H.E.; Fullarton, I.C.; De Souza, R.A.; Kilner, J.A.; Bouwmeester, H.J.M.; Burggraaf, A.J. Surface oxygen exchange of $\text{La}_{0.3}\text{Sr}_{0.7}\text{CoO}_{3-\delta}$. *Solid State Ion.* **1997**, *96*, 1–7. [[CrossRef](#)]
20. Yildiz, B. “Stretching” the energy landscape of oxides-Effects on electrocatalysis and diffusion. *MRS Bull.* **2014**, *39*, 147–156. [[CrossRef](#)]
21. Berenov, A.V.; Atkinson, A.; Kilner, J.A.; Bucher, E.; Sitte, W. Oxygen tracer diffusion and surface exchange kinetics in $\text{La}_{0.6}\text{Sr}_{0.4}\text{CoO}_{3-\delta}$. *Solid State Ion.* **2010**, *181*, 819–826. [[CrossRef](#)]
22. Carter, S.; Selcuk, A.; Chater, R.J.; Kajda, J.; Kilner, J.A.; Steele, B.C.H. Oxygen transport in selected nonstoichiometric perovskite-structure oxides. *Solid State Ion.* **1992**, *53*, 597–605. [[CrossRef](#)]
23. Lane, J.A.; Benson, S.J.; Waller, D.; Kilner, J.A. Oxygen transport in $\text{La}_{0.6}\text{Sr}_{0.4}\text{Co}_{0.2}\text{Fe}_{0.8}\text{O}_{3-\delta}$. *Solid State Ion.* **1999**, *121*, 201–208. [[CrossRef](#)]
24. Wang, L.; Merkle, R.; Maier, J.; Acartürk, T.; Starke, U. Oxygen tracer diffusion in dense $\text{Ba}_{0.5}\text{Sr}_{0.5}\text{Co}_{0.8}\text{Fe}_{0.2}\text{O}_{3-\delta}$ films. *Appl. Phys. Lett.* **2009**, *94*, 071908. [[CrossRef](#)]
25. Munnings, C.N.; Skinner, S.J.; Amow, G.; Whitfield, P.S.; Davidson, I.J. Oxygen transport in the $\text{La}_2\text{Ni}_{1-x}\text{Co}_x\text{O}_{4+\delta}$ system. *Solid State Ion.* **2005**, *176*, 1895–1901. [[CrossRef](#)]
26. Baumann, F.S.; Maier, J.; Fleig, J. The polarization resistance of mixed conducting SOFC cathodes: A comparative study using thin film model electrodes. *Solid State Ion.* **2008**, *179*, 1198–1204. [[CrossRef](#)]
27. Crumlin, E.J.; Ahn, S.J.; Lee, D.; Mutoro, E.; Biegalski, M.D.; Christen, H.M.; Shao-Horn, Y. Oxygen electrocatalysis on epitaxial $\text{La}_{0.6}\text{Sr}_{0.4}\text{CoO}_{3-\delta}$ perovskite thin films for solid oxide fuel cells. *J. Electrochem. Soc.* **2012**, *159*, F219–F225. [[CrossRef](#)]

28. LaO', G.J.; Ahn, S.J.; Crumlin, E.; Orikasa, Y.; Biegalski, M.D.; Christen, H.M.; Shao-Horn, Y. Catalytic activity enhancement for oxygen reduction on epitaxial perovskite thin films for solid-oxide fuel cells. *Angew. Chem.* **2010**, *49*, 5344–5347.
29. Santiso, J.; Burriel, M. Deposition and characterisation of epitaxial oxide thin films for SOFCs. *J. Solid State Electrochem.* **2011**, *15*, 985–1006. [[CrossRef](#)]
30. Lutchyn, R.M.; Sau, J.D.; Das Sarma, S. Majorana fermions and a topological phase transition in semiconductor-superconductor heterostructures. *Phys. Rev. Lett.* **2010**, *105*, 077001. [[CrossRef](#)]
31. Smadici, S.; Abbamonte, P.; Bhattacharya, A.; Zhai, X.; Jiang, B.; Rusydi, A.; Eckstein, J.N.; Bader, S.D.; Zuo, J.M. Electronic reconstruction at SrMnO₃-LaMnO₃ superlattice interfaces. *Phys. Rev. Lett.* **2007**, *99*, 196404. [[CrossRef](#)]
32. Chakhalian, J.; Freeland, J.W.; Srajer, G.; Stremper, J.; Khaliullin, G.; Cezar, J.C.; Charlton, T.; Dalglish, R.; Bernhard, C.; Cristiani, G.; et al. Magnetism at the interface between ferromagnetic and superconducting oxides. *Nat. Phys.* **2006**, *2*, 244–248. [[CrossRef](#)]
33. Sase, M.; Hermes, F.; Yashiro, K.; Sato, K.; Mizusaki, J.; Kawada, T.; Sakai, N.; Yokokawa, H. Enhancement of oxygen surface exchange at the hetero-interface of (La,Sr)CoO₃/(La,Sr)₂CoO₄ with PLD-layered films. *J. Electrochem. Soc.* **2008**, *155*, B793–B797. [[CrossRef](#)]
34. Chronos, A.; Vovk, R.V.; Goulatis, I.L.; Goulatis, L.I. Oxygen transport in perovskite and related oxides: A brief review. *J. Alloys Compd.* **2010**, *494*, 190–195. [[CrossRef](#)]
35. Kharton, V.V.; Viskup, A.P.; Kovalevsky, A.V.; Naumovich, E.N.; Marques, F.M.B. Ionic transport in oxygen-hyperstoichiometric phases with K₂NiF₄-type structure. *Solid State Ion.* **2001**, *143*, 337–353. [[CrossRef](#)]
36. Minh, N.Q. Ceramic fuel-cells. *J. Am. Ceram. Soc.* **1993**, *76*, 563–588. [[CrossRef](#)]
37. Minervini, L.; Grimes, R.W.; Kilner, J.A.; Sickafus, K.E. Oxygen migration in La₂NiO_{4+δ}. *J. Mater. Chem.* **2000**, *10*, 2349–2354. [[CrossRef](#)]
38. Opila, E.J.; Tuller, H.L.; Wuensch, B.J.; Maier, J. Oxygen tracer diffusion in La_{2-x}Sr_xCuO_{4-δ} single-crystals. *J. Am. Ceram. Soc.* **1993**, *76*, 2363–2369. [[CrossRef](#)]
39. Horita, T.; Yamaji, K.; Sakai, N.; Xiong, Y.; Yokokawa, H.; Kawada, T.J.I. Application of novel SIMS technique for imaging the active sites of oxygen reduction at the SOFC cathode/electrolyte interfaces. *Ionics* **2002**, *8*, 108–117. [[CrossRef](#)]
40. Horita, T.; Yamaji, K.; Sakai, N.; Yokokawa, H.; Weber, A.; Ivers-Tiffée, E. Oxygen reduction mechanism at porous La_{1-x}Sr_xCoO_{3-δ} cathodes/La_{0.8}Sr_{0.2}Ga_{0.8}Mg_{0.2}O_{2.8} electrolyte interface for solid oxide fuel cells. *Electrochim. Acta* **2001**, *46*, 1837–1845. [[CrossRef](#)]
41. Kamata, H.; Hosaka, A.; Mizusaki, J.; Tagawa, H. High temperature electrocatalytic properties of the SOFC air electrode La_{0.8}Sr_{0.2}MnO₃/YSZ. *Solid State Ion.* **1998**, *106*, 237–245. [[CrossRef](#)]
42. Opitz, A.K.; Schintlmeister, A.; Hutter, H.; Fleig, J. Visualization of oxygen reduction sites at Pt electrodes on YSZ by means of ¹⁸O tracer incorporation: The width of the electrochemically active zone. *Phys. Chem. Chem. Phys.* **2010**, *12*, 12734–12745. [[CrossRef](#)]
43. Østergård, M.J.L.; Mogensen, M. ac Impedance study of the oxygen reduction mechanism on La_{1-x}Sr_xMnO₃ in solid oxide fuel cells. *Electrochim. Acta* **1993**, *38*, 2015–2020. [[CrossRef](#)]
44. Robertson, N.L.; Michaels, J.N. Oxygen exchange on platinum electrodes in zirconia cells: Location of electrochemical reaction sites. *J. Electrochem. Soc.* **1990**, *137*, 129–135. [[CrossRef](#)]
45. Bouwmeester, H.J.M.; Kruidhof, H.; Burggraaf, A.J. Importance of the surface exchange kinetics as rate-limiting step in oxygen permeation through mixed-conducting oxides. *Solid State Ion.* **1994**, *72*, 185–194. [[CrossRef](#)]
46. Van der Haar, L.M.; den Otter, M.W.; Morskate, M.; Bouwmeester, H.J.M.; Verweij, H. Chemical diffusion and oxygen surface transfer of La_{1-x}Sr_xCoO_{3-δ} studied with electrical conductivity relaxation. *J. Electrochem. Soc.* **2002**, *149*, J41–J46. [[CrossRef](#)]
47. Baumann, F.S.; Fleig, J.; Habermeier, H.U.; Maier, J. Impedance spectroscopic study on well-defined (La,Sr)(Co,Fe)O_{3-δ} model electrodes. *Solid State Ion.* **2006**, *177*, 1071–1081. [[CrossRef](#)]
48. Jamnik, J.; Maier, J. Generalised equivalent circuits for mass and charge transport: Chemical capacitance and its implications. *Phys. Chem. Chem. Phys.* **2001**, *3*, 1668–1678. [[CrossRef](#)]
49. Yang, Y.L.; Chen, C.L.; Chen, S.Y.; Chu, C.W.; Jacobson, A.J. Impedance studies of oxygen exchange on dense thin film electrodes of La_{0.5}Sr_{0.5}CoO_{3-δ}. *J. Electrochem. Soc.* **2000**, *147*, 4001–4007. [[CrossRef](#)]

50. Endo, A.; Fukunaga, H.; Wen, C.; Yamada, K. Cathodic reaction mechanism of dense $\text{La}_{0.6}\text{Sr}_{0.4}\text{CoO}_3$ and $\text{La}_{0.81}\text{Sr}_{0.09}\text{MnO}_3$ electrodes for solid oxide fuel cells. *Solid State Ion.* **2000**, *135*, 353–358. [[CrossRef](#)]
51. Yang, Y.L.; Jacobson, A.J.; Chen, C.L.; Luo, G.P.; Ross, K.D.; Chu, C.W. Oxygen exchange kinetics on a highly oriented $\text{La}_{0.5}\text{Sr}_{0.5}\text{CoO}_{3-\delta}$ thin film prepared by pulsed-laser deposition. *Appl. Phys. Lett.* **2001**, *79*, 776–778. [[CrossRef](#)]
52. Sase, M.; Ueno, D.; Yashiro, K.; Kaimai, A.; Kawada, T.; Mizusaki, J. Interfacial reaction and electrochemical properties of dense $(\text{La,Sr})\text{CoO}_{3-\delta}$ cathode on YSZ (100). *J. Phys. Chem. Solids* **2005**, *66*, 343–348. [[CrossRef](#)]
53. Maier, J. Physical chemistry of ionic materials: Ions and electrons in solids. Wiley **2004**.
54. Fleig, J.; Maier, J. The polarization of mixed conducting SOFC cathodes: Effects of surface reaction coefficient, ionic conductivity and geometry. *J. Eur. Ceram. Soc.* **2004**, *24*, 1343–1347. [[CrossRef](#)]
55. Cai, Z.; Kuru, Y.; Han, J.W.; Chen, Y.; Yildiz, B. Surface electronic structure transitions at high temperature on perovskite oxides: The case of strained $\text{La}_{0.8}\text{Sr}_{0.2}\text{CoO}_3$ thin films. *J. Am. Chem. Soc.* **2011**, *133*, 17696–17704. [[CrossRef](#)]
56. Donner, W.; Chen, C.; Liu, M.; Jacobson, A.J.; Lee, Y.L.; Gadre, M.; Morgan, D. Epitaxial strain-induced chemical ordering in $\text{La}_{0.5}\text{Sr}_{0.5}\text{CoO}_{3-\delta}$ films on SrTiO_3 . *Chem. Mater.* **2011**, *23*, 984–988. [[CrossRef](#)]
57. Garcia-Barriocanal, J.; Rivera-Calzada, A.; Varela, M.; Sefrioui, Z.; Iborra, E.; Leon, C.; Pennycook, S.J.; Santamaria, J. Colossal ionic conductivity at interfaces of epitaxial $\text{ZrO}_2\text{:Y}_2\text{O}_3/\text{SrTiO}_3$ heterostructures. *Science* **2008**, *321*, 676–680. [[CrossRef](#)]
58. Schichtel, N.; Korte, C.; Hesse, D.; Janek, J. Elastic strain at interfaces and its influence on ionic conductivity in nanoscaled solid electrolyte thin films—Theoretical considerations and experimental studies. *Phys. Chem. Chem. Phys.* **2009**, *11*, 3043–3048. [[CrossRef](#)]
59. Wang, Z.W.; Shu, D.J.; Wang, M.; Ming, N.B. Diffusion of oxygen vacancies on a strained rutile TiO_2 (110) surface. *Phys. Rev. B* **2010**, *82*, 165309. [[CrossRef](#)]
60. Kushima, A.; Yip, S.; Yildiz, B. Competing strain effects in reactivity of LaCoO_3 with oxygen. *Phys. Rev. B* **2010**, *82*, 115435. [[CrossRef](#)]
61. Burriel, M.; Garcia, G.; Santiso, J.; Kilner, J.A.; Chater, R.J.; Skinner, S.J. Anisotropic oxygen diffusion properties in epitaxial thin films of $\text{La}_2\text{NiO}_{4+\delta}$. *J. Mater. Chem.* **2008**, *18*, 416–422. [[CrossRef](#)]
62. Ji, H.I.; Hwang, J.; Yoon, K.J.; Son, J.W.; Kim, B.K.; Lee, H.W.; Lee, J.H. Enhanced oxygen diffusion in epitaxial lanthanum–strontium–cobaltite thin film cathodes for micro solid oxide fuel cells. *Energy Environ. Sci.* **2013**, *6*, 116–120. [[CrossRef](#)]
63. Lee, D.; Grimaud, A.; Crumlin, E.J.; Mezghani, K.; Habib, M.A.; Feng, Z.; Hong, W.T.; Biegalski, M.D.; Christen, H.M.; Shao-Horn, Y. Strain influence on the oxygen electrocatalysis of the (100)-oriented epitaxial $\text{La}_2\text{NiO}_{4+\delta}$ thin films at elevated temperatures. *J. Phys. Chem. C* **2013**, *117*, 18789–18795. [[CrossRef](#)]
64. Kubicek, M.; Cai, Z.; Ma, W.; Yildiz, B.; Hutter, H.; Fleig, J. Tensile lattice strain accelerates oxygen surface exchange and diffusion in $\text{La}_{1-x}\text{Sr}_x\text{CoO}_{3-\delta}$ thin films. *ACS Nano* **2013**, *7*, 3276–3286. [[CrossRef](#)]
65. Lee, D.; Lee, Y.L.; Grimaud, A.; Hong, W.T.; Biegalski, M.D.; Morgan, D.; Shao-Horn, Y. Strontium influence on the oxygen electrocatalysis of $\text{La}_{2-x}\text{Sr}_x\text{NiO}_{4\pm\delta}$ ($0.0 \leq x_{\text{Sr}} \leq 1.0$) thin films. *J. Mater. Chem. A* **2014**, *2*, 6480–6487. [[CrossRef](#)]
66. Lee, D.; Lee, Y.L.; Wang, X.R.; Morgan, D.; Shao-Horn, Y. Enhancement of oxygen surface exchange on epitaxial $\text{La}_{0.6}\text{Sr}_{0.4}\text{Co}_{0.2}\text{Fe}_{0.8}\text{O}_{3-\delta}$ thin films using advanced heterostructured oxide interface engineering. *MRS Commun.* **2016**, *6*, 204–209. [[CrossRef](#)]
67. Sase, M.; Hermes, F.; Nakamura, T.; Yashiro, K.; Sato, K.; Mizusaki, J.; Kawada, T.; Sakai, N.; Yamaji, K.; Horita, T.; et al. Promotion of oxygen surface reaction at the hetero-interface of $(\text{La,Sr})\text{CoO}_3/(\text{La,Sr})_2\text{CoO}_4$. *ECS Trans.* **2007**, *7*, 1055–1060.
68. Yashiro, K.; Nakamura, T.; Sase, M.; Hermes, F.; Sato, K.; Kawada, T.; Mizusaki, J. Electrode performance at hetero-interface of perovskite-related oxides, $(\text{La,Sr})\text{CoO}_{3-\delta}/(\text{La,Sr})_2\text{CoO}_{4-\delta}$. *ECS Trans.* **2007**, *7*, 1287–1292.
69. Schlom, D.G.; Haeni, J.H.; Lettieri, J.; Theis, C.D.; Tian, W.; Jiang, J.C.; Pan, X.Q. Oxide nano-engineering using MBE. *Mater. Sci. Eng. B* **2001**, *87*, 282–291. [[CrossRef](#)]
70. Elam, J.W.; Groner, M.D.; George, S.M. Viscous flow reactor with quartz crystal microbalance for thin film growth by atomic layer deposition. *Rev. Sci. Instrum.* **2002**, *73*, 2981–2987. [[CrossRef](#)]
71. Lowndes, D.H.; Geohegan, D.B.; Puretzy, A.A.; Norton, D.P.; Rouleau, C.M. Synthesis of novel thin-film materials by pulsed laser deposition. *Science* **1996**, *273*, 898–903. [[CrossRef](#)]

72. Alfonso, E.; Olaya, J.; Cubillos, G. Thin film growth through sputtering technique and its applications. In *Crystallization—Science and Technology*; IntechOpen: London, UK, 2012.
73. Adler, S.B. Mechanism and kinetics of oxygen reduction on porous $\text{La}_{1-x}\text{Sr}_x\text{CoO}_{3-\delta}$ electrodes. *Solid State Ion.* **1998**, *111*, 125–134. [[CrossRef](#)]
74. Jiang, Y.; Wang, S.Z.; Zhang, Y.H.; Yan, J.W.; Li, W.Z. Electrochemical reduction of oxygen on a strontium doped lanthanum manganite electrode. *Solid State Ion.* **1998**, *110*, 111–119. [[CrossRef](#)]
75. Van Doorn, R.H.E.; Burggraaf, A.J. Structural aspects of the ionic conductivity of $\text{La}_{1-x}\text{Sr}_x\text{CoO}_{3-\delta}$. *Solid State Ion.* **2000**, *128*, 65–78. [[CrossRef](#)]
76. Lee, D.; Lee, Y.L.; Grimaud, A.; Hong, W.T.; Biegalski, M.D.; Morgan, D.; Shao-Horn, Y. Enhanced oxygen surface exchange kinetics and stability on epitaxial $\text{La}_{0.8}\text{Sr}_{0.2}\text{CoO}_{3-\delta}$ thin films by $\text{La}_{0.8}\text{Sr}_{0.2}\text{MnO}_{3-\delta}$ decoration. *J. Phys. Chem. C* **2014**, *118*, 14326–14334. [[CrossRef](#)]
77. Esquirol, A.; Brandon, N.P.; Kilner, J.A.; Mogensen, M. Electrochemical characterization of $\text{La}_{0.6}\text{Sr}_{0.4}\text{Co}_{0.2}\text{Fe}_{0.8}\text{O}_3$ cathodes for intermediate-temperature SOFCs. *J. Electrochem. Soc.* **2004**, *151*, A1847–A1855. [[CrossRef](#)]
78. Geary, T.C.; Lee, D.; Shao-Horn, Y.; Adler, S.B. Nonlinear impedance analysis of $\text{La}_{0.4}\text{Sr}_{0.6}\text{Co}_{0.2}\text{Fe}_{0.8}\text{O}_{3-\delta}$ thin film oxygen electrodes. *J. Electrochem. Soc.* **2016**, *163*, F1107–F1114. [[CrossRef](#)]
79. Jiang, S.P. A comparison of O_2 reduction reactions on porous $(\text{La,Sr})\text{MnO}_3$ and $(\text{La,Sr})(\text{Co,Fe})\text{O}_3$ electrodes. *Solid State Ion.* **2002**, *146*, 1–22. [[CrossRef](#)]
80. Katsuki, M.; Wang, S.; Dokiya, M.; Hashimoto, T. High temperature properties of $\text{La}_{0.6}\text{Sr}_{0.4}\text{Co}_{0.8}\text{Fe}_{0.2}\text{O}_{3-\delta}$ oxygen nonstoichiometry and chemical diffusion constant. *Solid State Ion.* **2003**, *156*, 453–461. [[CrossRef](#)]
81. Kuhn, M.; Fukuda, Y.; Hashimoto, S.; Sato, K.; Yashiro, K.; Mizusaki, J. Oxygen nonstoichiometry and thermo-chemical stability of perovskite-type $\text{La}_{0.6}\text{Sr}_{0.4}\text{Co}_{1-y}\text{Fe}_y\text{O}_{3-\delta}$ ($y = 0, 0.2, 0.4, 0.5, 0.6, 0.8, 1$) materials. *J. Electrochem. Soc.* **2013**, *160*, F34–F42. [[CrossRef](#)]
82. Lynch, M.E.; Yang, L.; Qin, W.T.; Choi, J.J.; Liu, M.F.; Blinn, K.; Liu, M.L. Enhancement of $\text{La}_{0.6}\text{Sr}_{0.4}\text{Co}_{0.2}\text{Fe}_{0.8}\text{O}_{3-\delta}$ durability and surface electrocatalytic activity by $\text{La}_{0.85}\text{Sr}_{0.15}\text{MnO}_{3\pm\delta}$ investigated using a new test electrode platform. *Energy Environ. Sci.* **2011**, *4*, 2249–2258. [[CrossRef](#)]
83. Tai, L.W.; Nasrallah, M.M.; Anderson, H.U.; Sparlin, D.M.; Sehlin, S.R. Structure and electrical-properties of $\text{La}_{1-x}\text{Sr}_x\text{Co}_{1-y}\text{Fe}_y\text{O}_3$ Part 1. The system $\text{La}_{0.8}\text{Sr}_{0.2}\text{Co}_{1-y}\text{Fe}_y\text{O}_3$. *Solid State Ion.* **1995**, *76*, 259–271. [[CrossRef](#)]
84. Steele, B.C.H.; Bae, J.M. Properties of $\text{La}_{0.6}\text{Sr}_{0.4}\text{Co}_{0.2}\text{Fe}_{0.8}\text{O}_{3-x}$ (LSCF) double layer cathodes on gadolinium-doped cerium oxide (CGO) electrolytes: II. Role of oxygen exchange and diffusion. *Solid State Ion.* **1998**, *106*, 255–261. [[CrossRef](#)]
85. Ingram, B.J.; Eastman, J.A.; Chang, K.C.; Kim, S.K.; Fister, T.T.; Perret, E.; You, H.; Baldo, P.M.; Fuoss, P.H. In situ X-ray studies of oxygen surface exchange behavior in thin film $\text{La}_{0.6}\text{Sr}_{0.4}\text{Co}_{0.2}\text{Fe}_{0.8}\text{O}_{3-\delta}$. *Appl. Phys. Lett.* **2012**, *101*, 051603. [[CrossRef](#)]
86. Lee, D.; Lee, Y.L.; Hong, W.T.; Biegalski, M.D.; Morgan, D.; Shao-Horn, Y. Oxygen surface exchange kinetics and stability of $(\text{La,Sr})_2\text{CoO}_{4\pm\delta}/\text{La}_{1-x}\text{Sr}_x\text{MO}_{3-\delta}$ ($M = \text{Co}$ and Fe) hetero-interfaces at intermediate temperatures. *J. Mater. Chem. A* **2015**, *3*, 2144–2157. [[CrossRef](#)]
87. Cho, S.Y.; Chung, Y.C.; Ahn, K.; Lee, J.H.; Kim, B.K.; Kim, H. Oxygen transport in epitaxial $\text{La}_{0.875}\text{Sr}_{0.125}\text{CoO}_{3-\delta}$ thin-film cathodes for solid oxide fuel cells: Roles of anisotropic strain. *Scr. Mater.* **2016**, *115*, 141–144. [[CrossRef](#)]
88. Gan, L.Y.; Akande, S.O.; Schwingenschlogl, U. Anisotropic O vacancy formation and diffusion in LaMnO_3 . *J. Mater. Chem. A* **2014**, *2*, 19733–19737. [[CrossRef](#)]
89. Kushima, A.; Yildiz, B. Role of lattice strain and defect chemistry on the oxygen vacancy migration at the $(8.3\% \text{Y}_2\text{O}_3\text{-ZrO}_2) / \text{SrTiO}_3$ hetero-interface: A first principles study. *ECS Trans.* **2009**, *25*, 1599–1609.
90. Mayeshiba, T.; Morgan, D. Strain effects on oxygen migration in perovskites. *Phys. Chem. Chem. Phys.* **2015**, *17*, 2715–2721. [[CrossRef](#)]
91. Petrie, J.R.; Jeen, H.; Barron, S.C.; Meyer, T.L.; Lee, H.N. Enhancing perovskite electrocatalysis through strain tuning of the oxygen deficiency. *J. Am. Chem. Soc.* **2016**, *138*, 7252–7255. [[CrossRef](#)]
92. Petrie, J.R.; Mitra, C.; Jeen, H.; Choi, W.S.; Meyer, T.L.; Reboledo, F.A.; Freeland, J.W.; Eres, G.; Lee, H.N. Strain control of oxygen vacancies in epitaxial strontium cobaltite films. *Adv. Funct. Mater.* **2016**, *26*, 1564–1570. [[CrossRef](#)]
93. Xu, T.; Shimada, T.; Araki, Y.; Wang, J.; Kitamura, T. Defect-strain engineering for multiferroic and magnetoelectric properties in epitaxial (110) ferroelectric lead titanate. *Phys. Rev. B* **2015**, *92*, 104106. [[CrossRef](#)]

94. Han, J.W.; Yildiz, B. Enhanced one dimensional mobility of oxygen on strained $\text{LaCoO}_3(001)$ surface. *J. Mater. Chem.* **2011**, *21*, 18983–18990. [[CrossRef](#)]
95. Hong, W.T.; Gadre, M.; Lee, Y.L.; Biegalski, M.D.; Christen, H.M.; Morgan, D.; Shao-Horn, Y. Tuning the spin state in LaCoO_3 thin films for enhanced high-temperature oxygen electrocatalysis. *J. Phys. Chem. Lett.* **2013**, *4*, 2493–2499. [[CrossRef](#)]
96. Lee, D.; Jacobs, R.; Jee, Y.; Seo, A.; Sohn, C.; Ievlev, A.V.; Ovchinnikova, O.S.; Huang, K.; Morgan, D.; Lee, H.N. Stretching epitaxial $\text{La}_{0.6}\text{Sr}_{0.4}\text{CoO}_{3-\delta}$ for fast oxygen reduction. *J. Phys. Chem. C* **2017**, *121*, 25651–25658. [[CrossRef](#)]
97. Rupp, G.M.; Kubicek, M.; Opitz, A.K.; Fleig, J. In situ impedance analysis of oxygen exchange on growing $\text{La}_{0.6}\text{Sr}_{0.4}\text{CoO}_{3-\delta}$ thin films. *ACS Appl. Energy Mater.* **2018**, *1*, 4522–4535. [[CrossRef](#)]
98. Hou, F.; Cai, T.Y.; Ju, S.; Shen, M.R. Half-metallic ferromagnetism via the interface electronic reconstruction in $\text{LaAlO}_3/\text{SrMnO}_3$ nanosheet superlattices. *ACS Nano* **2012**, *6*, 8552–8562. [[CrossRef](#)]
99. Rata, A.D.; Herklotz, A.; Nenkov, K.; Schultz, L.; Dörr, K. Strain-induced insulator state and giant gauge factor of $\text{La}_{0.7}\text{Sr}_{0.3}\text{CoO}_3$ films. *Phys. Rev. Lett.* **2008**, *100*, 076401. [[CrossRef](#)]
100. Lee, Y.L.; Kleis, J.; Rossmeis, J.; Shao-Horn, Y.; Morgan, D. Prediction of solid oxide fuel cell cathode activity with first-principles descriptors. *Energy Environ. Sci.* **2011**, *4*, 3966–3970. [[CrossRef](#)]
101. Zhu, Z.; Shi, Y.; Aruta, C.; Yang, N. Improving electronic conductivity and oxygen reduction activity in Sr-doped lanthanum cobaltite thin films: Cobalt valence state and electronic band structure effects. *ACS Appl. Energy Mater.* **2018**, *1*, 5308–5317. [[CrossRef](#)]
102. Yamazoe, N.; Teraoka, Y. Oxidation catalysis of perovskites — relationships to bulk structure and composition (valency, defect, etc.). *Catal. Today* **1990**, *8*, 175–199. [[CrossRef](#)]
103. Fierro, J.L.G.; Tejuca, L.G. Non-stoichiometric surface behaviour of LaMO_3 oxides as evidenced by XPS. *Appl. Surf. Sci.* **1987**, *27*, 453–457. [[CrossRef](#)]
104. Peña, M.A.; Fierro, J.L.G. Chemical structures and performance of perovskite oxides. *Chem. Rev.* **2001**, *101*, 1981–2018. [[CrossRef](#)]
105. Chavan, S.V.; Singh, R.N. Preparation, properties, and reactivity of lanthanum strontium ferrite as an intermediate temperature SOFC cathode. *J. Mater. Sci.* **2013**, *48*, 6597–6604. [[CrossRef](#)]
106. Simner, S.P.; Bonnett, J.F.; Canfield, N.L.; Meinhardt, K.D.; Shelton, J.P.; Sprenkle, V.L.; Stevenson, J.W. Development of lanthanum ferrite SOFC cathodes. *J. Power Sources* **2003**, *113*, 1–10. [[CrossRef](#)]
107. Petitjean, M.; Caboche, G.; Siebert, E.; Dessemond, L.; Dufour, L.C. $(\text{La}_{0.8}\text{Sr}_{0.2})(\text{Mn}_{1-y}\text{Fe}_y)\text{O}_{3\pm\delta}$ oxides for IT-SOFC cathode materials?: Electrical and ionic transport properties. *J. Eur. Ceram. Soc.* **2005**, *25*, 2651–2654. [[CrossRef](#)]
108. La O', G.J.; Shao-Horn, Y. Oxygen surface exchange kinetics on Sr-substituted lanthanum manganite and ferrite thin-film microelectrodes. *J. Electrochem. Soc.* **2009**, *156*, B816–B824. [[CrossRef](#)]
109. Wang, S.; Katsuki, M.; Dokiya, M.; Hashimoto, T. High temperature properties of $\text{La}_{0.6}\text{Sr}_{0.4}\text{Co}_{0.8}\text{Fe}_{0.2}\text{O}_{3-\delta}$ phase structure and electrical conductivity. *Solid State Ion.* **2003**, *159*, 71–78. [[CrossRef](#)]
110. Ralph, J.M.; Rossignol, C.; Kumar, R. Cathode materials for reduced-temperature SOFCs. *J. Electrochem. Soc.* **2003**, *150*, A1518–A1522. [[CrossRef](#)]
111. Perry Murray, E.; Sever, M.J.; Barnett, S.A. Electrochemical performance of $(\text{La,Sr})(\text{Co,Fe})\text{O}_3-(\text{Ce,Gd})\text{O}_3$ composite cathodes. *Solid State Ion.* **2002**, *148*, 27–34. [[CrossRef](#)]
112. Adler, S.B.; Lane, J.A.; Steele, B.C.H. Electrode kinetics of porous mixed-conducting oxygen electrodes. *J. Electrochem. Soc.* **1996**, *143*, 3554–3564. [[CrossRef](#)]
113. Chen, C.C.; Nasrallah, M.M.; Anderson, H.U.; Alim, M.A. Impedance response of $\text{La}_{0.6}\text{Sr}_{0.4}\text{Co}_{0.2}\text{Fe}_{0.8}\text{O}_3$ based electrochemical cells. *J. Electrochem. Soc.* **1995**, *142*, 491–496. [[CrossRef](#)]
114. Prestat, M.; Infortuna, A.; Korrodi, S.; Rey-Mermet, S.; Mural, P.; Gauckler, L.J. Oxygen reduction at thin dense $\text{La}_{0.52}\text{Sr}_{0.48}\text{Co}_{0.18}\text{Fe}_{0.82}\text{O}_{3-\delta}$ electrodes. *J. Electroceram.* **2007**, *18*, 111–120. [[CrossRef](#)]
115. Angoua, B.F.; Slamovich, E.B. Single solution spray pyrolysis of $\text{La}_{0.6}\text{Sr}_{0.4}\text{Co}_{0.2}\text{Fe}_{0.8}\text{O}_{3-\delta}-\text{Ce}_{0.8}\text{Gd}_{0.2}\text{O}_{1.9}$ (LSCF-CGO) thin film cathodes. *Solid State Ion.* **2012**, *212*, 10–17. [[CrossRef](#)]
116. Develos-Bagarinao, K.; Kishimoto, H.; De Vero, J.; Yamaji, K.; Horita, T. Effect of $\text{La}_{0.6}\text{Sr}_{0.4}\text{Co}_{0.2}\text{Fe}_{0.8}\text{O}_{3-\delta}$ microstructure on oxygen surface exchange kinetics. *Solid State Ion.* **2016**, *288*, 6–9. [[CrossRef](#)]
117. Hopper, E.M.; Perret, E.; Ingram, B.J.; You, H.; Chang, K.C.; Baldo, P.M.; Fuoss, P.H.; Eastman, J.A. Oxygen exchange in $\text{La}_{0.6}\text{Sr}_{0.4}\text{Co}_{0.2}\text{Fe}_{0.8}\text{O}_{3-\delta}$ thin-film heterostructures under applied electric potential. *J. Phys. Chem. C* **2015**, *119*, 19915–19921. [[CrossRef](#)]

118. Plonczak, P.; Søgaard, M.; Bieberle-Hütter, A.; Hendriksen, P.V.; Gauckler, L.J. Electrochemical characterization of $\text{La}_{0.58}\text{Sr}_{0.4}\text{Co}_{0.2}\text{Fe}_{0.8}\text{O}_{3-\delta}$ thin film electrodes prepared by pulsed laser deposition. *J. Electrochem. Soc.* **2012**, *159*, B471–B482. [[CrossRef](#)]
119. Armstrong, E.N.; Duncan, K.L.; Oh, D.J.; Weaver, J.F.; Wachsmann, E.D. Determination of surface exchange coefficients of LSM, LSCF, YSZ, GDC constituent materials in composite SOFC cathodes. *J. Electrochem. Soc.* **2011**, *158*, B492–B499. [[CrossRef](#)]
120. Dumaisnil, K.; Carru, J.C.; Fasquelle, D.; Mascot, M.; Rolle, A.; Vannier, R.N. Promising performances for a $\text{La}_{0.6}\text{Sr}_{0.4}\text{Co}_{0.8}\text{Fe}_{0.2}\text{O}_{3-\delta}$ cathode with a dense interfacial layer at the electrode-electrolyte interface. *Ionics* **2017**, *23*, 2125–2132. [[CrossRef](#)]
121. Jang, I.; Kim, C.; Kim, S.; Yoon, H.; Paik, U. Fabrication of nanoparticle networked $\text{La}_{0.6}\text{Sr}_{0.4}\text{Co}_{0.2}\text{Fe}_{0.8}\text{O}_{3-\delta}$ thin film layer between the cathode and electrolyte of solid oxide fuel cell by using a spin coating method. *ECS Trans.* **2017**, *78*, 741–745. [[CrossRef](#)]
122. Jang, I.; Kim, S.; Kim, C.; Yoon, H.; Song, T. Enhancement of oxygen reduction reaction through coating a nano-web-structured $\text{La}_{0.6}\text{Sr}_{0.4}\text{Co}_{0.2}\text{Fe}_{0.8}\text{O}_{3-\delta}$ thin-film as a cathode/electrolyte interfacial layer for lowering the operating temperature of solid oxide fuel cells. *J. Power Sources* **2018**, *392*, 123–128. [[CrossRef](#)]
123. Ruddlesden, S.N.; Popper, P. The compound $\text{Sr}_3\text{Ti}_2\text{O}_7$ and its structure. *Acta Crystallogr.* **1958**, *11*, 54–55. [[CrossRef](#)]
124. Brown, I.D. Modeling the structures of La_2NiO_4 . *Z. Kristall.* **1992**, *199*, 255–272. [[CrossRef](#)]
125. Sase, M.; Yashiro, K.; Sato, K.; Mizusaki, J.; Kawada, T.; Sakai, N.; Yamaji, K.; Horita, T.; Yokokawa, H. Enhancement of oxygen exchange at the hetero interface of $(\text{La},\text{Sr})\text{CoO}_3/(\text{La},\text{Sr})_2\text{CoO}_4$ in composite ceramics. *Solid State Ion.* **2008**, *178*, 1843–1852. [[CrossRef](#)]
126. Lee, Y.L.; Lee, D.; Wang, X.R.; Lee, H.N.; Morgan, D.; Shao-Horn, Y. Kinetics of oxygen surface exchange on epitaxial Ruddlesden-Popper phases and correlations to first-principles descriptors. *J. Phys. Chem. Lett.* **2016**, *7*, 244–249. [[CrossRef](#)]
127. Gopalakrishnan, J.; Colsmann, G.; Reuter, B. Studies on $\text{La}_{2-x}\text{Sr}_x\text{NiO}_4$ ($0 < x < 1$) system. *J. Solid State Chem.* **1977**, *22*, 145–149.
128. Bassat, J.M.; Burriel, M.; Wahyudi, O.; Castaing, R.; Ceretti, M.; Veber, P.; Weill, I.; Villesuzanne, A.; Grenier, J.C.; Paulus, W.; et al. Anisotropic oxygen diffusion properties in $\text{Pr}_2\text{NiO}_{4+\delta}$ and $\text{Nd}_2\text{NiO}_{4+\delta}$ single crystals. *J. Phys. Chem. C* **2013**, *117*, 26466–26472. [[CrossRef](#)]
129. Burriel, M.; Santiso, J.; Rossell, M.D.; Van Tendeloo, G.; Figueras, A.; Garcia, G. Enhancing total conductivity of $\text{La}_2\text{NiO}_{4+\delta}$ epitaxial thin films by reducing thickness. *J. Phys. Chem. C.* **2008**, *112*, 10982–10987. [[CrossRef](#)]
130. Garcia, G.; Burriel, M.; Bonanos, N.; Santiso, J. Electrical conductivity and oxygen exchange kinetics of $\text{La}_2\text{NiO}_{4+\delta}$ thin films grown by chemical vapor deposition. *J. Electrochem. Soc.* **2008**, *155*, P28–P32. [[CrossRef](#)]
131. Kharton, V.V.; Yaremchenko, A.A.; Shaula, A.L.; Patrakeev, M.V.; Naumovich, E.N.; Loginovich, D.I.; Frade, J.R.; Marques, F.M.B. Transport properties and stability of Ni-containing mixed conductors with perovskite- and K_2NiF_4 -type structure. *J. Solid State Chem.* **2004**, *177*, 26–37. [[CrossRef](#)]
132. Kim, G.T.; Wang, S.Y.; Jacobson, A.J.; Yuan, Z.; Chen, C.L. Impedance studies of dense polycrystalline thin films of $\text{La}_2\text{NiO}_{4+\delta}$. *J. Mater. Chem.* **2007**, *17*, 1316–1320. [[CrossRef](#)]
133. Burriel, M.; Téllez, H.; Chater, R.J.; Castaing, R.; Veber, P.; Zaghrioui, M.; Ishihara, T.; Kilner, J.A.; Bassat, J.M. Influence of crystal orientation and annealing on the oxygen diffusion and surface exchange of $\text{La}_2\text{NiO}_{4+\delta}$. *J. Phys. Chem. C.* **2016**, *120*, 17927–17938. [[CrossRef](#)]
134. Yamada, A.; Suzuki, Y.; Saka, K.; Uehara, M.; Mori, D.; Kanno, R.; Kiguchi, T.; Mauvy, F.; Grenier, J.C. Ruddlesden-Popper-type epitaxial film as oxygen electrode for solid-oxide fuel cells. *Adv. Mater.* **2008**, *20*, 4124. [[CrossRef](#)]
135. Tsvetkov, N.; Lu, Q.; Chen, Y.; Yildiz, B. Accelerated oxygen exchange kinetics on $\text{Nd}_2\text{NiO}_{4+\delta}$ thin films with tensile strain along c-axis. *ACS Nano* **2015**, *9*, 1613–1621. [[CrossRef](#)] [[PubMed](#)]
136. Kim, G.; Wang, S.; Jacobson, A.J.; Chen, C.L. Measurement of oxygen transport kinetics in epitaxial $\text{LaNiO}_{4+\delta}$ thin films by electrical conductivity relaxation. *Solid State Ion.* **2006**, *177*, 1461–1467. [[CrossRef](#)]
137. Xie, W.; Lee, Y.L.; Shao-Horn, Y.; Morgan, D. Oxygen point defect chemistry in Ruddlesden-Popper oxides $(\text{La}_{1-x}\text{Sr}_x)_2\text{MO}_{4\pm\delta}$ ($\text{M} = \text{Co}, \text{Ni}, \text{Cu}$). *J. Phys. Chem. Lett.* **2016**, *7*, 1939–1944. [[CrossRef](#)] [[PubMed](#)]
138. Goodenough, J.B.; Manthiram, A. Crystal-chemistry and superconductivity of the copper oxides. *J. Solid State Chem.* **1990**, *88*, 115–139. [[CrossRef](#)]

139. Gozar, A.; Logvenov, G.; Kourkoutis, L.F.; Bollinger, A.T.; Giannuzzi, L.A.; Muller, D.A.; Bozovic, I. High-temperature interface superconductivity between metallic and insulating copper oxides. *Nature* **2008**, *455*, 782. [[CrossRef](#)]
140. Hoppner, J.; Stahn, J.; Niedermayer, C.; Malik, V.K.; Bouyanfif, H.; Drew, A.J.; Rossle, M.; Buzdin, A.; Cristiani, G.; Habermeier, H.U.; et al. Giant superconductivity-induced modulation of the ferromagnetic magnetization in a cuprate-manganite superlattice. *Nat. Mater.* **2009**, *8*, 315–319. [[CrossRef](#)]
141. Opila, E.J.; Tuller, H.L. Thermogravimetric analysis and defect models of the oxygen nonstoichiometry in $\text{La}_{2-x}\text{Sr}_x\text{CuO}_{4-y}$. *J. Am. Ceram. Soc.* **1994**, *77*, 2727–2737. [[CrossRef](#)]
142. Meyer, T.L.; Jacobs, R.; Lee, D.; Jiang, L.; Freeland, J.W.; Sohn, C.; Egami, T.; Morgan, D.; Lee, H.N. Strain control of oxygen kinetics in the Ruddlesden-Popper oxide $\text{La}_{1.85}\text{Sr}_{0.15}\text{CuO}_4$. *Nat. Commun.* **2018**, *9*, 92. [[CrossRef](#)] [[PubMed](#)]
143. Yashiro, K.; Nakamura, T.; Sase, M.; Hermes, F.; Sato, K.; Kawada, T.; Mizusaki, J. Composite cathode of perovskite-related oxides, $(\text{La,Sr})\text{CoO}_{3-\delta}/(\text{La,Sr})_2\text{CoO}_{4-\delta}$, for solid oxide fuel cells. *Electrochem. Solid State Lett.* **2009**, *12*, B135–B137. [[CrossRef](#)]
144. Chen, Y.; Téllez, H.; Burriel, M.; Yang, F.; Tsvetkov, N.; Cai, Z.; McComb, D.W.; Kilner, J.A.; Yildiz, B. Segregated chemistry and structure on (001) and (100) Surfaces of $(\text{La}_{1-x}\text{Sr}_x)_2\text{CoO}_4$ override the crystal anisotropy in oxygen exchange kinetics. *Chem. Mater.* **2015**, *27*, 5436–5450. [[CrossRef](#)]
145. Chen, J.; Liang, F.L.; Chi, B.; Pu, J.; Jiang, S.P.; Jian, L. Palladium and ceria infiltrated $\text{La}_{0.8}\text{Sr}_{0.2}\text{Co}_{0.5}\text{Fe}_{0.5}\text{O}_{3-\delta}$ cathodes of solid oxide fuel cells. *J. Power Sources* **2009**, *194*, 275–280. [[CrossRef](#)]
146. Han, J.W.; Yildiz, B. Mechanism for enhanced oxygen reduction kinetics at the $(\text{La,Sr})\text{CoO}_{3-\delta}/(\text{La,Sr})_2\text{CoO}_{4+\delta}$ hetero-interface. *Energy Environ. Sci.* **2012**, *5*, 8598–8607. [[CrossRef](#)]
147. Liu, M.F.; Ding, D.; Blinn, K.; Li, X.X.; Nie, L.F.; Liu, M. Enhanced performance of LSCF cathode through surface modification. *Int. J. Hydrogen Energy* **2012**, *37*, 8613–8620. [[CrossRef](#)]
148. Crumlin, E.J.; Mutoro, E.; Ahn, S.J.; la O', G.J.; Leonard, D.N.; Borisevich, A.; Biegalski, M.D.; Christen, H.M.; Shao-Horn, Y. Oxygen reduction kinetics enhancement on a heterostructured oxide surface for solid oxide fuel cells. *J. Phys. Chem. Lett.* **2010**, *1*, 3149–3155. [[CrossRef](#)]
149. Atkinson, A.; Ramos, T. Chemically-induced stresses in ceramic oxygen ion-conducting membranes. *Solid State Ion.* **2000**, *129*, 259–269. [[CrossRef](#)]
150. Zhao, C.; Liu, X.; Zhang, W.; Zheng, Y.; Li, Y.; Yu, B.; Wang, J.; Chen, J. Measurement of oxygen reduction/evolution kinetics enhanced $(\text{La,Sr})\text{CoO}_3/(\text{La,Sr})_2\text{CoO}_4$ hetero-structure oxygen electrode in operating temperature for SOCs. *Int. J. Hydrog. Energy* **2018**. [[CrossRef](#)]
151. Feng, Z.; Yacoby, Y.; Hong, W.T.; Zhou, H.; Biegalski, M.D.; Christen, H.M.; Shao-Horn, Y. Revealing the atomic structure and strontium distribution in nanometer-thick $\text{La}_{0.8}\text{Sr}_{0.2}\text{CoO}_{3-\delta}$ grown on (001)-oriented SrTiO_3 . *Energy Environ. Sci.* **2014**, *7*, 1166–1174. [[CrossRef](#)]
152. Feng, Z.; Crumlin, E.J.; Hong, W.T.; Lee, D.; Mutoro, E.; Biegalski, M.D.; Zhou, H.; Bluhm, H.; Christen, H.M.; Shao-Horn, Y. In situ studies of the temperature-dependent surface structure and chemistry of single-crystalline (001)-oriented $\text{La}_{0.8}\text{Sr}_{0.2}\text{CoO}_{3-\delta}$ perovskite thin films. *J. Phys. Chem. Lett.* **2013**, *4*, 1512–1518. [[CrossRef](#)] [[PubMed](#)]
153. Lou, X.Y.; Wang, S.Z.; Liu, Z.; Yang, L.; Liu, M.L. Improving $\text{La}_{0.6}\text{Sr}_{0.4}\text{Co}_{0.2}\text{Fe}_{0.8}\text{O}_{3-\delta}$ cathode performance by infiltration of a $\text{Sm}_{0.5}\text{Sr}_{0.5}\text{CoO}_{3-\delta}$ coating. *Solid State Ion.* **2009**, *180*, 1285–1289. [[CrossRef](#)]
154. Nie, L.F.; Liu, M.F.; Zhang, Y.J.; Liu, M.L. $\text{La}_{0.6}\text{Sr}_{0.4}\text{Co}_{0.2}\text{Fe}_{0.8}\text{O}_{3-\delta}$ cathodes infiltrated with samarium-doped cerium oxide for solid oxide fuel cells. *J. Power Sources* **2010**, *195*, 4704–4708. [[CrossRef](#)]
155. Chen, H.; Guo, Z.; Zhang, L.A.; Li, Y.; Li, F.; Zhang, Y.; Chen, Y.; Wang, X.; Yu, B.; Shi, J.M.; et al. Improving the electrocatalytic activity and durability of the $\text{La}_{0.6}\text{Sr}_{0.4}\text{Co}_{0.2}\text{Fe}_{0.8}\text{O}_{3-\delta}$ cathode by surface modification. *ACS Appl. Mater. Interfaces* **2018**, *10*, 39785–39793. [[CrossRef](#)]

